

2018-02

# Three-dimensional dynamics of baroclinic tides over a seamount

Vlasenko, Vasyl

<http://hdl.handle.net/10026.1/10845>

---

10.1002/2017JC013287

Journal of Geophysical Research: Oceans

American Geophysical Union

---

*All content in PEARL is protected by copyright law. Author manuscripts are made available in accordance with publisher policies. Please cite only the published version using the details provided on the item record or document. In the absence of an open licence (e.g. Creative Commons), permissions for further reuse of content should be sought from the publisher or author.*

# Three-dimensional dynamics of baroclinic tides over a seamount

Vasiliy Vlasenko<sup>1</sup>, Nataliya Stashchuk<sup>1</sup>, and W. Alex M. Nimmo-Smith<sup>1</sup>

---

Vasiliy Vlasenko, School of Biological and Marine Sciences, Plymouth University, Plymouth, PL4 8AA, UK (vvlasenko@plymouth.ac.uk)

<sup>1</sup>School of Biological and Marine Sciences, Plymouth University, Plymouth, PL4 8AA, UK.

**Abstract.**

The Massachusetts Institute of Technology general circulation model is used for the analysis of baroclinic tides over Anton Dohrn Seamount (ADS), in the North Atlantic. The model output is validated against in-situ data collected during the 136-th cruise of the RRS “James Cook” in May-June 2016. The observational data set includes velocity time series recorded at two moorings as well as temperature, salinity and velocity profiles collected at 22 hydrological stations. Synthesis of observational and model data enabled the reconstruction of the details of baroclinic tidal dynamics over ADS. It was found that the baroclinic tidal waves are generated in the form of tidal beams radiating from the ADS periphery to its centre, focusing tidal energy in a surface layer over the seamount’s summit. This energy focusing enhances subsurface water mixing and the local generation of internal waves. The tidal beams interacting with the seasonal pycnocline generate short-scale internal waves radiating from the ADS centre. An important ecological outcome from this study concerns the pattern of residual currents generated by tides. The rectified flows over ADS have the form of a pair of dipoles, cyclonic and anti-cyclonic eddies located at the seamount’s periphery. These eddies are potentially an important factor in local larvae dispersion and their escape from ADS.

## 1. Introduction

21 The oceanic floor contains around 12000 seamounts [*Wessel et al.*, 2010] that play an  
22 important role in tidal energy conversion and the formation of local ecological communi-  
23 ties. Seamounts act as natural obstacles for currents enhancing tidal energy dissipation  
24 and water mixing. There is evidence that seamounts form hotspots of biological activity  
25 in the oceans [*Lavelle and Mohn*, 2010; *Morato et al.*, 2010]. Analysis done by *Rogers*  
26 [1994] indicates that higher species richness detected at seamounts compared to coastal  
27 or oceanic areas can be a consequence of enhanced oceanic dynamical activity in these  
28 areas [*Henry et al.*, 2014].

29 The primary aims of the 136-th cruise of the RRS “James Cook” (hereafter JC136) to  
30 the North East Atlantic in May-June 2016 were (i) to find a connection between the pop-  
31 ulations of corals in the bathyal zone on different seamounts, and (ii) to find a correlation  
32 between coral diversity and oceanic processes near seamounts (tides, currents, internal  
33 waves, eddies, etc.). For these purposes the ship was equipped with a remotely operating  
34 vehicle (ROV) ISIS that conducted surveys and collected samples of biological species  
35 from the Anton Dorn, Rockal Bank, George Bligh, and Rosemary Seamounts, as well as  
36 from the Wyville Thomson Ridge. The principal part of the oceanographic measurements  
37 included deployment of two moorings and CTD-LADCP sampling in the area of Anton  
38 Dorn Seamount (ADS), located to the west of Scotland in the central part of the Rockall  
39 Trough. This seamount, or table-mount guyot, is a former volcano with nearly circular  
40 shape and about 40 km in diameter, Figure 1. ADS rises approximately 1800 m above the  
41 bottom with minimum depth in its centre of about 530 m.

42 A large number of theoretical and experimental papers have been published on dynamical processes over seamounts, e.g. barotropic and baroclinic tides, generation of internal waves, mixing, response to stationary currents, formation of residual circulation, eddies, etc. An overview of the most significant publications can be found in *Vlasenko et al.* [2013]. The primary goal of the present paper is to report a new set of observational data collected during JC136 near ADS. These data were used for setting a numerical model and its further validation. An overall goal of these model efforts was to investigate the tidal regime around ADS that took place during the JC136 cruise. The comprehensive model output allowed us to build up a complete picture of possible motions developing in the area, specifically, baroclinic tidal energy focusing over the bank, local generation of internal waves due to interaction of tidal beams with the seasonal pycnocline, and the generation of residual currents and their possible implication for larvae dispersion.

54 The paper is organised as follows. The measurement techniques and collected data are presented in Section 2, along with the model set-up. The next section reports the effect of the focusing of baroclinic tidal energy over the ADS summit. The mechanism of local generation of internal waves is discussed in Section 4. Tidally generated residual currents and their possible implications for larvae dispersion are analysed in Section 5. Finally, Section 6 summarises all principal findings.

## 2. Measurements and model set up

### 2.1. Observational data set

60 Figure 1 shows the scheme of the field experiment conducted on JC136 cruise. The observational campaign included 18 CTD stations, deployment of two moorings, M1 and M2, and four dives of the ROV ISIS. Note that CTD stations 4-19 located at the edge of

63 steep topography were repeated at the same site (yo-yo) on 19th May 2016 when ROV  
 64 dives were suspended due to bad weather conditions. At the end of the cruise (on 17th  
 65 June 2016) three CTD stations, 41-43, were conducted along the cross-bank transect  
 66 shown in Figure 1. A Lowered Acoustic Doppler Current Profiler (LADCP) was mounted  
 67 at the CTD rosette, so vertical profiles of horizontal velocities were recorded at each  
 68 station. The obtained data were processed with the LDEO LADCP Processing Software  
 69 developed by *Visbeck* [2002].

70 Moorings M1 and M2 were equipped with an upward-looking 75 kHz Acoustic Doppler  
 71 Current Profilers (ADCP) and a 600 KHz downward-looking ADCP for measuring the  
 72 flow regime in the bottom boundary layer. Details of moorings instruments are provided  
 73 in Table 1. Table 2 shows the coordinates of ROV dives 270, 271, 272, and 292 that were  
 74 used for modelling larvae dispersion. The collected data set was complemented with a  
 75 velocity time series recorded by a vessel mounted ADCP (150kHz) during ROV dive 296.

## 2.2. The model

76 The fully nonlinear nonhydrostatic Massachusetts Institute of Technology general circu-  
 77 lation model (MITgcm, *Marshall et al.* [1997]) was used for modelling the wave dynamics  
 78 near ADS. The semi-diurnal  $M_2$  tidal harmonics predominates in the area [*Egbert and*  
 79 *Erofeeva*, 2002], so we restricted our analysis by considering only this tidal constituent.  
 80 The tidal forcing was activated in the model using an external software package added  
 81 to the MITgcm code that sets a tidal potential in the RHS of the momentum balance  
 82 equations. Two tidal components were introduced as follows [*Stashchuk et al.*, 2017]

$$83 \quad U = A \sin(\omega t + \phi), \quad V = B \sin(\omega t), \quad (1)$$

84 where  $U$  and  $V$  are zonal and meridional water discharge, respectively,  $\omega$  is the tidal  
85 frequency, and  $\phi$  is the phase lag that controls the tidal ellipse inclination. The main part  
86 of the field campaign was conducted during the transition from neap to spring tide, so for  
87 setting the tide in the model we used  $A=50\text{ m}^2\text{ s}^{-1}$ ,  $B=100\text{ m}^2\text{ s}^{-1}$ , and  $\phi = \pi/4.1$ , which  
88 provides a good coincidence with the ellipses of the inverse tidal model TPXO8.1 [*Egbert*  
89 *and Erofeeva*, 2002], Figure 2 a. A non-slip boundary condition was used at the bottom.

90 The model domain included  $768\times 794$  grid points. Its central part with  $512\times 538$  grid  
91 points and horizontal resolution  $\Delta x = \Delta y=115\text{ m}$  was used for the analysis. The lateral  
92 grid areas that included 118 grid points were added at each side of the model domain. Here  
93 the grid step was increased telescopically from 115 m in the central part to 5500 m towards  
94 the boundaries. Such a grid stretching allows one to radiate internal waves from the central  
95 area without their backward reflection from the boundaries. Another 10 boundary steps  
96 of the model domain at the periphery were added to release the barotropic tidal waves  
97 from the area. Here the grid step increased to  $2\cdot 10^8\text{ m}$  at the model boundary. Such  
98 a combination of a two-step telescopic grids eliminates reflection of both barotropic and  
99 internal waves from the outer boundaries during the ten days of the numerical experiment.

100 The vertical grid step was  $\Delta z = 10\text{ m}$  which provided quite a detailed resolution of tidally  
101 induced baroclinic fields. The fluid stratification was taken from CTD data recorded at  
102 station 1. The buoyancy frequency profile (blue line) is shown in Figure 2 b together with  
103 the smoothed profile (the red line).

104 The coefficients of horizontal viscosity were taken at the level of  $10^{-2}\text{ m}^2\text{ s}^{-1}$ . The  
105 vertical turbulent closure for the coefficients of vertical viscosity  $\nu$  and diffusivity  $\kappa$  was  
106 provided by the Richardson number dependent parametrisation, [*Pacanowski and Philan-*

107 *der*, 1981]:

$$\begin{aligned} \nu &= \frac{\nu_0}{(1 + \mu \text{Ri})^n} + \nu_b, \\ \kappa &= \frac{\nu}{(1 + \mu \text{Ri})} + \kappa_b. \end{aligned} \tag{2}$$

108  
 109 Here Ri is the Richardson number,  $\text{Ri} = N^2(z)/(u_z^2 + v_z^2)$ , and  $N^2(z) = -(g/\rho)(\partial\rho/\partial z)$   
 110 is the buoyancy frequency ( $g$  is the acceleration due to gravity, and  $\rho$  is the density),  
 111  $u$  and  $v$  are zonal and meridional velocities;  $\nu_b=10^{-5} \text{ m}^2 \text{ s}^{-1}$  and  $\kappa_b=10^{-5} \text{ m}^2 \text{ s}^{-1}$  are the  
 112 background parameters,  $\nu_0=1.5 \cdot 10^{-2} \text{ m}^2 \text{ s}^{-1}$ ,  $\mu=5$  and  $n=1$  are the adjustable parameters.  
 113 Such a parametrisation increases coefficients  $\nu$  and  $\kappa$  in the areas where the Richardson  
 114 number is small to take into account the mixing processes induced by shear instabilities  
 115 and breaking internal waves. A systematic analysis of the sensitivity of the model output  
 116 to the parameters  $\nu_b$ ,  $\kappa_b$ ,  $\nu_0$ ,  $\mu$ , and  $n$  was conducted in [*Stashchuk and Hutter*, 2001].  
 117 It was found that with the above mentioned parameters formula (2) keeps the diffusivity  
 118 and viscosity at the level sufficient for the model stability. On the other hand, this level  
 119 of mixing and viscosity does not affect substantially the internal wave fields.

### 3. Tidal beams and energy focusing

120 We start our analysis with consideration of the velocity profiles recorded at CTD stations  
 121 41-43, Figure 1. The vertical profiles of instantaneous horizontal velocity  $\sqrt{u^2 + v^2}$  are  
 122 shown in Figures 3 a, 3 b, and 3 c by thick lines. These profiles clearly show evidence of  
 123 local velocity maxima located at different depths at stations 41-43. Specifically, Figure 3 a,  
 124 shows intensification of the surface currents at 100 m depth at station 43, just over the top  
 125 of ADS. The deepest maximum was recorded at 750 m depth at station 41 conducted at  
 126 the bank edge, Figure 3 c. In between, at station 42, the maximum of horizontal velocity  
 127 was found in the intermediate layer at 330 m depth, Figure 3 b.



128 A series of model-based sampling was arranged in a similar way to the observations, i.e.  
129 at the positions of CTD stations 41-43. Twelve vertical profiles of  $\sqrt{u^2 + v^2}$  spanning the  
130 CTD sampling time (an approximate duration of CTD samplings in the cruise was one  
131 hour) with 5-min time interval are shown in Figures 3 a, 3 b, and 3 c by thin light lines.  
132 Comparison of  $\sqrt{u^2 + v^2}$  profiles reveals that the positions of the extrema of the observed  
133 and model predicted profiles coincide. The level of theoretical and experimental amplitude  
134 velocities in these layers is also in a good agreement except probably the surface 200 m  
135 layer at station 43. The 50-100% inconsistency between theoretical and experimental  
136 profiles visible in the surface layer in Figures 3 a could be a consequence of a surface  
137 current that existed in the area during the field experiment, but which was not set in the  
138 model because of the lack of the observational data for its validation. Another reason  
139 for the reported inconsistency could be imperfection of the LADCP processing procedure  
140 [Visbeck, 2002] which underestimates currents near sea surface. This issue was discussed  
141 by Aleinik *et al.* [2007] who showed that the error in the velocity in the surface layer can  
142 be as large as 0.06-0.08 m s<sup>-1</sup>. Thus, taking into account this reasoning one can conclude  
143 that the model reproduces the wave dynamics in the ADS area correctly.

144 The reason for the reported velocity maxima at different depths can be explained by  
145 considering the spatial distribution of the amplitude of the horizontal velocities  $\sqrt{u^2 + v^2}$   
146 over one tidal cycle which is shown in Figure 3 d for the transect a-a (see Figure 1).  
147 This figure reveals evidence of two tidal beams generated at the sharp edges of the bank  
148 topography (at points A and B). They propagate upward and meet at the centre of the  
149 bank in the subsurface 200 m layer. The tidal-beam (or T-beam) interpretation of Figure

150 3 d is confirmed by the positions of the curves

$$151 \quad \int \frac{dz}{\alpha(z)} = \pm x + \text{const}, \quad \alpha(z) = \sqrt{\frac{\omega^2 - f^2}{N^2(z) - \omega^2}}, \quad (3)$$

152 shown in Figure 3 d by dashed lines. In this equation  $x$  and  $z$  are horizontal and vertical  
 153 coordinates,  $f$  is the Coriolis parameter, and  $N(z)$  is the buoyancy frequency. In fact,  
 154 dashed contours in Figure 3 d are the characteristic lines of the wave equation

$$155 \quad w_{xx} - \alpha^2(z)w_{zz} = 0, \quad (4)$$

156 where  $w$  is the vertical wave velocity. Coincidence of these lines with zones of velocity  
 157 maxima confirms a T-beam origin of the latter.

158 ADS is a circular guyot, Figure 1. One can assume that the T-beam mechanism of  
 159 generation of internal waves works also in all other cross-sections around ADS (a similar  
 160 case was considered by *Baines* [2007] for a symmetrical cylindrical seamount). As a  
 161 result of the seamount symmetry, the tidal energy propagating from many sites at the  
 162 bank periphery to its centre focuses over the top of ADS where station 43 was located.  
 163 From theoretical predictions a large area of high concentration of tidal energy should be  
 164 expected just over the seamount summit, which is obviously evident in Figure 3 d in the  
 165 surface 200 m layer.

166 Additional observational evidence of the T-beam generation can be found in the mooring  
 167 time series. According to Figure 3 d, both moorings, M1 and M2, were deployed in the  
 168 area where the T-beam could be recorded as a strong amplification of horizontal velocities  
 169 at depths around 800 m. In other words, the tidal beam should be seen in the moorings  
 170 velocity time series, as well. Figures 4 a and 4 c clearly show intensification of zonal and  
 171 meridional velocities in the bottom layer, specifically, below 700 m depth for mooring M1.

172 The model time series were recorded with a 20 s time interval at the position of mooring  
173 M1. They are presented in Figures 4 b (zonal velocity) and 4 d (meridional velocity).  
174 Comparison of the left and right patterns in Figure 4 shows their consistency.

175 Similar time series recorded at mooring M2 and reproduced numerically for the same  
176 time span are shown in Figure 5. The model predicts that the position of the tidal beam  
177 at this mooring should be at depths between 800 m and 1000 m, Figure 3 d. Figure 5  
178 demonstrates intensification of the tidal velocity in this layer, both in observational and  
179 model time series. The only difference between moorings M1 and M2 is that the latter  
180 was deployed deeper than M1, i.e. at the 1200 m isobath. According to the tidal beam  
181 position shown in Figure 3 d, no substantial currents at mooring M2 below 1000 m depth  
182 are expected. This is exactly what Figure 5 demonstrates, both in observations and in  
183 the model predictions.

184 Analysis of the mooring data can be complemented by considering vertical oscillations.  
185 Figure 6 presents vertical velocities recorded at both moorings, M1 and M2, and predicted  
186 by the model. This figure reveals tidal periodicity which is clearly visible in the mooring  
187 M2 time series (panel c). This strong tidal signal recorded in the 700-1000 m layer is  
188 associated with the tidal beam discussed above. In addition to that, one can identify  
189 also a large number of positive and negative short-term pulses. They are present both in  
190 observational and model time series and cover a large part of the water column. Joint  
191 analysis of vertical velocities with model predicted temperature time series presented in  
192 Figures 6 b and 6 d by black solid lines (isotherms are shown with  $0.2^\circ$  interval) reveals a  
193 strong correlation of short-term pulses evident in velocity records with vertical displace-

194 ments of isotherms in the seasonal thermocline produced by short period internal waves.  
195 The latter appear in packets with tidal periodicity indicating their tidal origin.

196 Two classes of internal waves visible in Figures 6 b and 6 d, i.e. short period packets  
197 and long term semi-diurnal waves, are separated in space occupying different parts of  
198 the water column. Short-period internal waves are mostly seen in the surface layer (that  
199 coincides with the seasonal thermocline), whereas long-period semidiurnal oscillations  
200 (classified above as evidence of the tidal beam) exist mostly below 600 m depth with  
201 largest amplitude at the depths of the main pycnocline, Figure 2.

202 Two different classes of internal waves generated in the ADS area are visible also in  
203 Figures 7 and 8. Figure 7 a represents a time series of the temperature profiles recorded  
204 on 19-th of May 2016 as repeated casts (yo-yo) with roughly 40 min time interval between  
205 samplings, and Figure 7 c shows this data as a set of vertical profiles. Figures 7 b and  
206 7 d show similar time series and the yo-yo temperature profiles produced by the model.  
207 One of the conclusions that can be drawn from the comparison of the in-situ collected  
208 data and the model output is their similarity which testifies an ability of the model to  
209 reproduce wave dynamics in the ADS area. This remark concerns consistency of the  
210 temperature records above 600 m depth, both in experimental and theoretical profiles,  
211 and their variability below 700 m depth.

212 Such a diversity of the temperature profiles below 600-metre depth can be explained in  
213 terms of vertical oscillations developed in the layer occupied by the tidal beam. Simple  
214 estimations based on Figure 7 a show that vertical displacements of isotherms from their  
215 stationary position can exceed 100 m. Bearing in mind that the yo-yo station was con-  
216 ducted at the periphery of ADS where the tidal beam is located below 600 m, one can

217 conclude that recorded variability of the temperature profiles in this layer (visible also in  
218 Figure 3) can be treated as evidence of the tidal beam discussed above.

219 Quite a different wave dynamics were observed in the surface layer. Figures 6 b and  
220 6 d show packets of short-period internal waves in the sub-surface layer predicted by the  
221 model. In the field experiment both ADCPs were unable to capture signals from the  
222 sub-surface layer (see Figures 4 a, 4 c; 5 a, 5 c; 6 a, 6 c). However, the ship-mounted ADCP  
223 was active during ROV missions, and the time series of the meridional and zonal velocities  
224 recorded during dive 296 are shown in Figures 8 a and b. Similar model predicted time  
225 series for the positions of moorings M1 and M2 are presented in Figures 8 c-f providing  
226 evidence of short period internal wave packets in the upper 250 m. The numerical model  
227 predicts their propagation northward, i.e. from mooring M1 to mooring M2. The velocity  
228 time series recorded by the ship mounted ADCP also confirms their northward propaga-  
229 tion in the area of moorings M1 and M2, see Figure 1. Bearing in mind that the bottom  
230 topography over the ADS summit is quite flat (Figures 1-3) and the total depth there is  
231 about 600 m, it is quite unlikely that the recorded short period internal waves were gener-  
232 ated over the top of the seamount according to a standard mechanism of tide-topography  
233 interaction. Clarification of the conditions for their generation is an objective of the next  
234 section.

## 4. Mechanisms of generation of internal waves

### 4.1. Local generation of internal waves

235 A relatively simple way to identify the potential locations of internal tide generation  
236 is to follow the methodology suggested by *Baines* [1982] localising the positions of the

237 maxima of the internal body force (IBF). In a two-dimensional  $(x, z)$  case the IBF is:

$$238 \quad \text{IBF} = \rho_0 u_{\text{tide}} H(x) z \frac{N^2(z)}{\omega} \left[ \frac{1}{H(x)} \right]_x. \quad (5)$$

239 Here  $u_{\text{tide}}$  is the amplitude of the barotropic tidal current;  $H(x)$  is the bottom profile;  
 240  $\rho_0$  is the mean density. In our case, the spatial distribution of the IBF in the meridional  
 241 across-bank section is presented in Figure 9 a.

242 It is clear from the IBF normalized distribution that the maximum of tidal energy  
 243 conversion (generation of internal tides) should take place over the seamount's flanks,  
 244 specifically, in the areas with centres  $57.23^\circ\text{N}$  at the south and  $57.62^\circ\text{N}$  at the north of  
 245 ADS. Note that the latitude  $57.62^\circ\text{N}$  is located just between moorings M1 and M2. Thus,  
 246 assuming the generation of the short period wave packets recorded during the ROV's dive  
 247 296 (shown in Figure 8), specifically in the area of the IBF maximum, these packets should  
 248 propagate in opposite directions at moorings M1 and M2. However, according to Figures  
 249 8 b and 8 d, they propagate in the same direction, i.e. northward. Taking into account a  
 250 one-hour time lag between arrival of the waves at moorings M1 and M2, Figures 8 b and  
 251 8 d, these waves should propagate from somewhere near the bank summit. Based solely  
 252 on the distance between the moorings and the recorded time lag one can estimate the  
 253 horizontal phase speed of the packet as  $c=0.74 \text{ m s}^{-1}$  which looks quite realistic for the  
 254 considered area (see also estimates below).

## 4.2. Lee wave mechanism

255 Another possible scenario for short-period waves generation could be a lee-wave mech-  
 256 anism, which usually takes place near abrupt changes of bottom topography. Specifically,  
 257 internal lee waves are generated downstream of the bottom topography by a strong su-

258 percritical tidal flow. They are released and propagate upstream when tidal flow slackens.  
 259 The feasibility of lee wave generation appears when the Froude number,  $Fr = u_{\text{tide}}/c$ , is  
 260 equal to or larger than 1. The phase speed  $c$  of internal lee waves is calculated from the  
 261 boundary value problem (BVP) for short-scale internal waves [Vlasenko *et al.*, 2005]

$$262 \quad \Phi_{zz} + \frac{N^2(z)}{c^2}\Phi = 0, \quad \Phi(-H) = \Phi(0) = 0.$$

263 Here the eigen function  $\Phi$  is the vertical structure function of internal waves. The estima-  
 264 tion of  $Fr$  for the ADS area has shown that its maximum value hardly exceeds 0.4, which  
 265 is insufficient for the lee wave mechanism to be realistic. It is interesting that the value  
 266 of the phase speed for the first baroclinic mode in the area of M1 and M2 varies between  
 267  $0.6 \text{ m s}^{-1}$  and  $0.9 \text{ m s}^{-1}$ , which is close to the phase speed of the wave packet calculated in  
 268 previous subsection.

### 4.3. T-beam generation mechanism

269 The above analysis has shown that neither IBF theory, nor the lee-wave mechanism  
 270 can explain the origin of the short-period internal waves propagating from the seamount  
 271 centre. Another hypothesis to be tested is the “local” generation of internal waves due  
 272 to the interaction of tidal beams with the seasonal pycnocline (hereafter, the T-beam  
 273 generation mechanism). The possibility of such a scenario can be concluded from the  
 274 analysis of Figure 3 where two tidal beam systems generated over ADS are clearly seen.  
 275 In space these beams follow the characteristic lines (3) of the wave equation (4). Figure 9 a  
 276 shows two families of characteristic lines (lines AD and BC) for the transect along  $11.1^\circ\text{W}$   
 277 latitude that crosses the ADS centre. The characteristic lines touch the bottom at points  
 278 A and B where their inclination coincides with the bottom steepness and where the tidal

279 beams are generated (see also Figure 3 d). As discussed above, the tidal beams propagating  
280 upward from the ADS periphery meet in the subsurface layer over the seamount's top (in  
281 the area between points C and D) where they hit the seasonal pycnocline. The latter  
282 starts to oscillate vertically with tidal frequency producing a series of progressive internal  
283 waves radiating from the centre of generation [Gerkema, 2001].

284 The process of local T-beam generation can be demonstrated using the Hovmöller di-  
285 agram, Figure 9 b. Here the model predicted evolution of the 12°C (equilibrium depth  
286 31 m) isotherm along the 11.1°W transect is presented at one hour intervals with time  
287 increasing from the top to the bottom. The ADS profile is shown here at the bottom of  
288 the figure. To visualise the wave evolution, the leading waves in each packet are connected  
289 by straight red lines. The wave trajectories clearly show that internal waves originate in  
290 the middle of ADS, specifically in the area of the C-D section, confirming the idea of local  
291 T-beam generation of internal waves due to interaction of tidal beams with the pycnocline.  
292 As was shown in *Vlasenko and Stashchuk* [2006, 2015], due to changing hydrological con-  
293 ditions and radial divergence, waves propagating seaward weaken in amplitude and can  
294 transform into different wave forms including high baroclinic modes [Vlasenko, 1994].

295 Note that the two-dimensional interpretation of local generation given above is not  
296 always applicable [Vlasenko *et al.*, 2014]. It can be extended to many other transects  
297 across the bank making the presentation substantially three-dimensional. For the three-  
298 dimensional analysis we use the amplitude of  $\sqrt{u^2 + v^2}$  at the free surface, Figure 10 a.  
299 Its spatial distribution shows the location of the T-beam generation and the main routes  
300 of the propagating waves. In Figure 10 a the wave fronts can be traced as the areas with  
301 the largest velocity values. They are seen as red arcs that radiate from the areas around



302 the seamount summit marked by letters C and D. The latter coincide with the positions  
 303 of C and D shown in Figures 9 a and 9 b.

304 The intensity of the velocity amplitudes of the generated waves is not evenly distributed  
 305 in space. It predominates mostly in the direction of the orientation of the major semi-  
 306 axis of tidal ellipses shown in Figure 10 a. This predominance of north-east and south-  
 307 west orientation of internal wave radiation can be explained also in terms of tidal energy  
 308 conversion discussed above, specifically, considering the positions of the generation of tidal  
 309 beams with respect to the topography. Figure 10 b shows amplitudes of horizontal velocity  
 310  $\sqrt{u^2 + v^2}$  10 m above the bottom. The position of points A and B in this graph is the  
 311 same as that shown in Figure 9 a. As one can see, these areas are the most energetic  
 312 in terms of tidal activity. In conjunction with Figures 3 d, 9 a, 10 a one can conclude  
 313 that focusing of baroclinic tidal energy over ADS summit triggers the mechanism of local  
 314 T-beam generation of internal waves in the area.

315 Another confirmation of local generation of internal waves over the ADS summit due to  
 316 the T-beam mechanism was found in a series of numerical experiments with an idealised  
 317 seamount

$$318 \quad H(x, y) = 1500 - 3000 \exp\{-[(x - x_s)^2 + (y - y_s)^2]/2500\}$$

319 where  $x_s$  and  $y_s$  are the coordinates of its centre. The seamount's height,  $H(x, z)$ , was  
 320 cut off at 700 m depth (minimum depth over ADS), and the sharp edges were smoothed  
 321 by moving average across the topography from the seamount centre to its periphery using  
 322 ten neighbouring grid points (Figure 11). The tidal parameters in these experiments were  
 323  $A = B = 100 \text{ m}^2 \text{ s}^{-1}$ , and  $\phi = \pi/2$  which turn the tidal ellipse (1) into a perfect circle.

324 The upper panel of Figure 11 shows the sea surface displacements produced by internal  
325 waves over this symmetrical table seamount after 57 hours of model time. Analysis of  
326 the wave fronts' structure and their spatial evolution reveals that the strongest waves  
327 are generated within the red dotted circle, i.e. in a region above the flat bottom from  
328 which they propagate radially decreasing in amplitude as spiral-type waves. Thus Figure  
329 11 confirms that the only possible explanation for these waves generation is the T-beam  
330 mechanism.

331 Maximum isotherm displacements in the epicentre of the generation area reach 20 m  
332 (see also Figure 6 b), which is several times smaller than the internal tidal oscillations  
333 in the tidal beams ( $\sim 100$  m). Parameters of the short-scale internal waves generated by  
334 tidal beams over idealized seamount or in the centre of ADS (these waves are visible  
335 in Figures 6, 8, 9, 11) can be sensitive to the level of the background mixing and the  
336 model resolution. Analysis of the sensitivity of the model output to the coefficient of the  
337 horizontal diffusion and grid step is presented in Appendix B.

#### 4.4. Implication for water mixing

338 It is expected that tidally generated internal waves can modify the background stratifica-  
339 tion by inducing mixing. Zones with strong mixing can be identified using the Richardson  
340 number  $Ri$ . According to *Miles* [1961] and *Howard* [1961], some level of mixing (turbu-  
341 lence) is expected in regions where the Richardson number  $Ri$  drops below  $1/4$  at least  
342 for a short period of time. *Abarbanel et al.* [1984] showed later that flows can be unstable  
343 even with  $Ri > 1/4$ , so for the qualitative analysis below we will take  $Ri = 1$  as a threshold  
344 for possible mixing events.

345 Figure 12a shows the area of the minimal Richardson numbers over one tidal cycle  
 346 along the transect a-a, Figure 1, where Ri drops below 1. This pattern is overlaid with  
 347 the amplitudes of horizontal velocities  $\sqrt{u^2 + v^2}$  to depict the positions of the tidal beams.  
 348 The  $0.2 \text{ m s}^{-1}$  isoline is shown by a solid black line. The smallest values of the Richardson  
 349 number are seen in the place where two tidal beams intersect between 50 m and 400 m  
 350 depths just in the centre over the seamount summit. According to Figure 2 b, the buoyancy  
 351 frequency here drops to  $0.0013 \text{ s}^{-1}$ , so strong vertical velocity shears associated with tidal  
 352 beams can reduce the Richardson number in this layer below the critical level.

353 An obvious indicator for mixing processes can be the difference  $\Delta T$  between the initial  
 354 background temperature  $T_0$  and the temperature  $\langle T \rangle$  modified by the wave mixing

$$355 \quad \Delta T = \langle T \rangle - T_0.$$

356 Here  $\langle T \rangle$  is the temperature field averaged over one tidal period. Figure 12 b presents  
 357 the temperature difference  $\Delta T$  produced by internal wave mixing along section a-a (Figure  
 358 1) over five tidal periods. It shows a considerable drop of the temperature (up to  $0.3^\circ$ ) in  
 359 the surface layer and a similar temperature rise just below this layer. This temperature  
 360 evolution can be treated in terms of internal wave activity that intensifies vertical mixing  
 361 in the seasonal pycnocline. As it was shown in Figure 10 a, the areas of enhanced internal  
 362 wave mixing are not evenly distributed in space. The temperature change  $\Delta T$  at the  
 363 depth of 30 m occupies a larger area to the south-south-west of the ADS summit than  
 364 anywhere else, Figure 12 c. This happens because of the strongest T-beam generation of  
 365 internal waves in this area.

366 As observational evidence of the intensification of local water mixing over the top of  
 367 ADS due to internal waves, the temperature profile recorded at CTD station 43, which

368 was inside a simulated region of cooling shown in Figure 12 c, reveals substantially lower  
369 temperature in the surface layer in comparison with those measured at CTD stations 41  
370 and 42 (Figure 12 d). This result is in agreement with the satellite observations (NASA  
371 Giovanni Web Portal <https://giovanni.gsfc.nasa.gov/giovanni/>) of the sea surface tem-  
372 perature (SST) collected by the MODIS-Aqua satellite. The SST anomalies calculated  
373 as a deviation from a long-term (years 2003-2016) mean May-August SST are shown in  
374 Figure 13. Large-scale zonal and meridional gradients have been subtracted from the SST  
375 field using a two-dimensional third-order polynomial. A very large area with SST more  
376 than  $0.1^{\circ}\text{C}$  lower than the surrounding area is located just over ADS (Figure 13). This  
377 feature resulting from enhanced vertical mixing can be treated in terms of the mechanism  
378 of baroclinic tidal energy focussing discussed above.

## 5. Residual tidal currents

379 In addition to internal waves, residual currents are also generated by periodical tidal  
380 flow over variable topography. These currents can be quite strong exceeding  $10\text{ cm s}^{-1}$  over  
381 the Malin Sea slope/shelf [*Stashchuk et al.*, 2017] or even more than  $20\text{ cm s}^{-1}$ , around the  
382 area of Georges Bank [*Loder*, 1980].

383 As distinct from shelf/slope areas where residual tidal currents normally take the form  
384 of along-slope flows [*Huthnance*, 1973] in three dimensions a periodically alternating tidal  
385 flow interacting with a seamount generates a dipole of eddies and density anomalies rotat-  
386 ing around the seamount [*Haidvogel et al.*, 1993]. Note, however, that the tidal forcing in  
387 the latter model was activated by a periodic barotropic discharge prescribed at one open  
388 boundary, whereas three other boundaries were taken as rigid walls. Such an approach  
389 results in the generation of standing waves instead of progressive waves and inertial os-

390 cillations that do not reproduce real tidal flow over an isolated bank located in the open  
391 sea.

392 To determine the structure of the residual currents over ADS, we configured the model  
393 for an idealised Gaussian bank and calculated the residual tidal fields both for homoge-  
394 neous and stratified fluids. The results are presented in the Appendix. As is shown there,  
395 an oscillating tidal flow generates two pairs of quasi-stationary cyclonic and anticyclonic  
396 eddies. A similar structure of residual currents over a Gaussian-type underwater bank  
397 was also reported by *Pingree and Maddock* [1980], who modelled a system of vertically  
398 integrated equations with quadratic terms for vertical viscosity. The intensity of these  
399 eddies is sensitive to the parameters of the tidal ellipses, specifically, to the length of the  
400 minor axis. The numerical experiments with the Gaussian seamount have shown that  
401 the smaller the minor axis, the stronger the residual currents. Water stratification also  
402 introduces some important effects changing the position of the eddies (for details see the  
403 Appendix).

404 These results obtained for an idealised bank are quite useful for interpretation of the spa-  
405 tial structure and evolution of the residual currents generated over real three-dimensional  
406 topographies. Figure 14 a shows the structure of the residual currents in the ADS area  
407 which resembled the picture of two eddy dipoles generated over an idealised seamount,  
408 Figure A.2 b, in particular. Of course, the imperfect asymmetric shape of the ADS to-  
409 pography results in violation of the symmetry of this pattern.

410 The transect of the residual zonal and meridional velocities along the Ellett Line (a  
411 regular annual CTD section across the Rockall Trough that includes ADS that has been  
412 sustained since 1975, [www.o-snap.org](http://www.o-snap.org)) are shown in Figures 14 b and 14 c. The spatial

413 structure of these model-predicted residual currents and their intensity are consistent with  
414 that recorded in-situ in mid-June 2009, [*Sherwin et al.*, 2015]. Figure 14 shows that in  
415 the vertical direction the eddies extend from the surface to the bottom of the seamount  
416 having mostly constant velocity over the whole water column.

### 5.1. Biological implications

417 Recent investigations by *Henry et al.* [2014] around Hebrides Terrace Seamount (North-  
418 East Atlantic ocean) have suggested that internal tides may enhance biological diversity  
419 on this and adjacent seamounts in the Rockall Trough. As shown above, oceanic tides  
420 generate internal waves, residual currents, and eddies around ADS, which can facilitate  
421 larvae dispersion between adjacent seamounts.

422 An underwater survey of ADS conducted using the ROV revealed a wide variety of  
423 biological species (sponges, corals, etc) in different parts at the ADS summit. It is clear  
424 that dynamical processes developing in the area can have strong effect on larvae dispersion.  
425 To understand possible larvae trajectories we used a passive tracer approach assuming that  
426 the larvae can be considered as floating particles transported by currents. To predict the  
427 positions of particles at some designated moments of time we used a Lagrangian approach  
428 with a method of multivariate interpolation on a 3-dimensional regular grid based on 5-  
429 minute model outputs of the three velocity components. The prediction time chosen for  
430 these experiments was 40 days which equals the time span required for larvae of marine  
431 corals to complete their life cycle [*Larsson et al.*, 2014]. (Nematocysts appear when larvae  
432 are 30 days old and if nematocysts are used for primary anchoring, this could indicate  
433 that larvae are capable to settle at this time. The larvae survived for a maximum 57 days  
434 in the laboratory.)

435 A large number of experiments revealed several realistic scenarios of larvae dispersion.  
436 In general, the vast majority of particles moved around the bank transported by residual  
437 currents. They were deposited at different places giving birth to new local colonies of  
438 corals. Some particles escape from the bank and can be considered as a potential source  
439 for wider spreading in the marine environment. We illustrate here the most interesting  
440 trajectories of four particular experiments. The particles started their journey from four  
441 different positions where the ROV conducted its dives, Figure 1. Specifically, one particle  
442 started from the seamount summit (dive 272), and three others from the northern flank  
443 of ADS (dives 270, 271, and 296). Geographically their positions were very close to each  
444 other, although due to steep topography they started at very different depths, i.e. at  
445 800 m, 1000 m, and 1100 m.

446 Figure 15 a shows a plan view of the trajectories of the particles overlapped with the field  
447 of residual currents, and Figure 15 b represents the particle tracks in three dimensions.  
448 The complex structure of the residual currents around the bank has a clear effect on  
449 the particle dispersion. Particles marked by green and red (dives 296 and 270) moved  
450 clockwise and the particle coloured with blue (dive 271) propagated counter-clockwise.  
451 Two particles in the north-east part left the seamount with strong outgoing currents.  
452 Another couple of particles do the same but at the south-western part of seamount.  
453 Figure 15 b shows that trajectories of particles are quite complicated in three dimensions.  
454 They show the potential for larvae to change depth with ascending or descending currents  
455 generated around the seamount, which is quite important for their wider dispersion.

## 6. Conclusions

456 The most significant results from the present study on investigation of tidal dynamics  
457 around Anton Dohrn Seamount can be split into three categories:

- 458 • **Baroclinic tidal energy focusing over the seamount's summit**

459 The ADS flanks are supercritical in terms of baroclinic tide generation (Figures 3 d and  
460 9 a). These are the necessary conditions for baroclinic tidal beam generation [*Vlasenko*  
461 *et al.*, 2005]. These beams propagate from the bank periphery to its centre focusing  
462 tidal energy over the top, similar to the mechanism of tidal energy focusing in canyons  
463 [*Vlasenko et al.*, 2016]. This mechanism resembles the effect of focusing in optical lenses.  
464 As a result, a large area of high internal tidal energy is created just over the seamount  
465 summit. This energy focusing, Figures 3 d, can have a great implication on water mixing  
466 over the top of seamounts and local generation of internal waves (T-beam generation).

- 467 • **Local T-beam generation**

468 The local generation of internal waves by tidal beams focusing in the ADS centre and  
469 their interaction with the seasonal pycnocline is confirmed in this study. Long ago this  
470 effect, called “local generation”, was discovered by *Pingree and Mardell* [1981, 1985] who  
471 were probably the first who observed this effect in-situ. The physical explanation of this  
472 process was given by *Gerkema* [2001]. The novel element of our study is that local T-beam  
473 generation is confirmed for a circular bank, specifically, over its centre where tidal beams  
474 intersect as a result of energy focusing. Taking into account that there are more than  
475 12000 seamounts in World's Oceans [*Wessel et al.*, 2010] the conclusions of the present  
476 study may be relevant to many other sites around the world.



477     • **Residual currents, eddies**

478     The most interesting ecological outcome from this study concerns the pattern of the  
479     residual currents generated by tides interacting with an isolated seamount. This effect  
480     resulting from tidal rectification along 2-dimensional topography was explained by *Huth-*  
481     *nance* [1973] and *Loder* [1980]. In application to a 3D object like ADS this theory predicts  
482     generation of two dipoles of cyclonic and anti-cyclonic eddies located at the seamount's  
483     periphery, *Stashchuk et al.* [2017]. They can be an important factor in coral larvae disper-  
484     sion including their escape from the seamount and travel to other banks of the World's  
485     Ocean.

## Appendix A: Residual tidal currents over an idealized Gaussian bank

486 The theory of tidally induced residual flows over an inclined bottom was developed  
 487 by *Huthnance* [1973] and modified by *Loder* [1980] who compared the theoretically pre-  
 488 dicted slope currents with numerical outputs for the area of Georges Bank. More recent  
 489 numerical experiments conducted by *Flexas et al.* [2015] have shown that the effect of  
 490 tidally generated residual slope currents can be one of the major driving forces for water  
 491 circulation in the Weddell-Scotia confluence, the principal area for formation of the global  
 492 meridional overturning circulation. The effect of tidally induced residual currents was  
 493 reviewed by *Stashchuk et al.* [2017] who conducted a systematic comparison analysis of  
 494 the model predicted slope currents with a theoretical formulae developed similar to *Huth-*  
 495 *nance* [1973] and *Loder* [1980]. Consistency of numerical and analytical solutions testifies  
 496 to the fact that the effect of tidally induced residual currents is quite remarkable and  
 497 should be taken into account in the analysis of water circulation in many areas. Below  
 498 we provide an analysis of the residual flows generated over an idealized Gaussian bank.  
 499 These experiments can shed light on the dynamics we can expect in the ADS area. The  
 500 shape of the bank for these experiments was taken as follows:

$$H(x, y) = 1000 - 400 \exp\{ -[(x - x_s)^2 + (y - y_s)^2]/800 \}, \quad (\text{A1})$$

502 where  $H(x, y)$  is the bottom profile and  $x_s$  and  $y_s$  are the coordinates of the seamount's  
 503 centre. The tidal currents were set in the model according to (1) with  $A = B = 100 \text{ m}^2 \text{ s}^{-1}$   
 504 (close to the discharge considered in the main series of runs). The configuration of tidal  
 505 ellipses was set by the phase  $\phi$ :  $\phi = 0$  corresponds to a periodical reversal flow, whereas  
 506  $\phi = \pi/2$  defines a perfect circle. The tidal phase  $\phi$  between 0 and  $\pi/2$  sets a tidal ellipse.

## A1. Barotropic response

507 In homogeneous fluids the tidally induced along-slope residual current  $v^c$  over a merid-  
 508 ionally oriented continental slope can be calculated using the following formula [*Stashchuk*  
 509 *et al.*, 2017]:

$$510 \quad v^c = \frac{AB \cos(\phi)}{2C_D \sqrt{A^2 + B^2}} \frac{1}{H(x)} \frac{\partial H(x)}{\partial x}. \quad (\text{A2})$$

511 Here  $H(x)$  is the bottom profile across the slope, and  $C_d = 0.013$ . Applying this formulae  
 512 to a singular circular object like the Gaussian seamount defined by (A1), one should take  
 513 into account the orientation of the bottom gradient as well. An accurate correction of  
 514 (A2) that takes into account the bottom orientation and the coordinate transforms was  
 515 provided in *Stashchuk et al.* [2017]. Considering positions at the periphery of the bank  
 516 and moving around it along isobaths this formulae predicts that the residual along-bank  
 517 slope current should change its sign four times depending on the location of the quadrant  
 518 where it is applied. As a result of this spatial variability, four eddies are expected to be  
 519 generated over the bank according to this analysis. This is exactly what the MITgcm  
 520 predicts for the Gaussian-type bank (A1).

521 Figure A.1 shows patterns of residual currents (middle row) and the vorticity  $u_y - v_x$   
 522 (bottom row) at a depth of 600 m for three different tidal configurations. A reversal tidal  
 523 flow mostly typical for weak rotation is presented in the left column ( $\phi = 0$ ), the mid-  
 524 latitude conditions are reproduced in the middle column ( $\phi = \pi/4$ ), and the case of strong  
 525 rotation is shown in the right column ( $\phi = \pi/2$ ). It is clear from Figure A.1 that the  
 526 MITgcm predicts the generation of four eddies over the seamount top: two cyclonic eddies  
 527 arranged along the major tidal semi-axis, and two anti-cyclonic eddies whose positions are

528 consistent with the direction of the minor semi-axis. The vorticity patterns also clearly  
529 show the location of two pairs of cyclonic and anti-cyclonic eddies.

530 It is interesting that formulae (A2) predicts zero residual currents for the case of a  
531 complete symmetry with  $\phi = \pi/2$ . This conclusion is consistent with the MITgcm output  
532 that does not predict significant residual currents for an axisymmetric case (right column).

## A2. Baroclinic effects

533 Stratification introduces quite a drastic reconfiguration of the structure of the residual  
534 flows. Figure A.2 shows a spatial distribution of the residual currents over the Gaussian  
535 bank overlaid with vertical velocities at a depth of 600 m obtained for homogeneous (Figure  
536 A.2 a) and stratified (Figure A.2 b) fluids. The stratification is that shown in Figure 2 b.  
537 For this experiment the same tidal parameters as above were taken, i.e.  $A = B = 100 \text{ m}^2 \text{ s}^{-1}$   
538 and  $\phi = 0$ .

539 Comparison of Figures A.2 a and A.2 b shows that they are quite different. The baro-  
540 clinic residual currents suppress the barotropic signal and reconfigure the entire spatial  
541 structure. First of all, the strongest currents are oriented now in the direction of the  
542 major axis of the tidal ellipse. In fact, this is the direction of propagation of the strongest  
543 internal waves generated over the bank and radiated from it. The position of the four  
544 eddies has also been changed. They were turned counter-clockwise by the angle of  $\pi/4$  to  
545 be consistent with the direction of internal wave propagation.

546 An even more drastic change has been introduced to the vertical velocity field. It does  
547 not resemble the barotropic case at all; the velocity patterns in both cases are completely  
548 different. First of all, the baroclinic vertical velocity currents are ten times stronger.  
549 Secondly, the strongest downwelling area is located just over the top of the bank, not at

550 its the periphery as in the barotropic case. And finally, the positive upward water fluxes  
551 are located on either sides of the downwelling area. Overall, the baroclinic residual tidal  
552 signal looks much stronger.

## Appendix B: Sensitivity to background mixing and grid resolution

553 Relatively high horizontal diffusion can reduce wave amplitudes. In the model the hor-  
554 izontal diffusion is introduced both explicitly by setting the coefficient of the horizontal  
555 diffusion as an input parameter (equal to  $0.01 \text{ m}^2\text{s}^{-1}$  in our case) and implicitly by set-  
556 ting the horizontal resolution which defines the numerical diffusion. The latter is always  
557 difficult for estimation based solely on the model output. However, in some cases it can  
558 be calculated accurately comparing an analytical solution of the diffusion equation and  
559 the model output from dye release experiments [*Stashchuk et al.*, 2014].

560 In order to investigate sensitivity of the model output to the diffusion coefficient and  
561 horizontal resolution in our case a series of extra numerical experiments was conducted  
562 with 60 m and 200 m horizontal resolution and  $0.1 \text{ m}^2\text{s}^{-1}$  coefficient of horizontal diffusion.  
563 The main conclusion from these experiments was that the characteristics of generated  
564 short-scale waves are nearly the same in all conducted experiments. This result on the  
565 consistency of all model outputs can be explained in terms of the concept of effective  
566 horizontal diffusion induced by generated internal waves. In some cases the effective  
567 diffusion can be much higher than the background and numerical diffusions. Based on the  
568 theory developed by *Young et al.* [1982], shear currents can increase the horizontal diffusion  
569 due to vertical diapycnal mixing. The formulae for the calculation of the coefficient of the

570 effective horizontal diffusion coefficient  $K_e$  reads

$$K_e = K_h + \frac{1}{2\omega^2} \left( \frac{du}{dz} \right)^2 \kappa. \quad (\text{B1})$$

571 Here  $du/dz$  is the velocity shear;  $\omega$  is the frequency of the oscillating tidal current;  $K_h$   
 572 and  $\kappa$  are the coefficients of the background horizontal and vertical diffusivity, respec-  
 573 tively (for the details of this theory we refer the reader to the original paper). The  
 574 coefficient of vertical diffusivity  $\kappa$  is set in the model by the *Pacanowski and Philander*  
 575 [1981] parametrisation (2). The mean value of this coefficient for the whole area over the  
 576 ADS summit was calculated by time and space averaging of all instant  $\kappa$  profiles over  
 577 one tidal period. As it was found, the vertical mixing was maximal in the surface 50 m  
 578 layer; the coefficient  $\kappa$  here was close to the maximal value set in the parametrisation (2).  
 579 Below this depth  $\kappa$  drops to  $0.005 \text{ m}^2\text{s}^{-1}$  in the layer between 50 and 100 m depth, and  
 580 to  $10^{-3} \text{ m}^2\text{s}^{-1}$  between 100 and 300 m depth. Having the model output for the horizontal  
 581 velocity shear, the contribution of the second term in (B1) to  $K_e$  was calculated. It was  
 582 found that  $K_e$  was 3 times larger than  $K_h$  in the layer 100-200 m depth, and 15 larger  
 583 than  $K_h$  in the subsurface 50-100 m layer. This overwhelming predominance of the wave  
 584 induced horizontal diffusion over the background and numerical diffusions is the reason  
 585 why the model was not sensitive to the choice of  $K_h$  and the grid resolution.

586 **Acknowledgments.** This work was supported by the UK NERC grant NE/K011855/1.  
 587 The authors would like to thank the captain, the crew and the ROV ISIS  
 588 team working during the JC136 cruise. The used data are available at  
 589 [https://figshare.com/articles/Untitled\\_Item/5472451](https://figshare.com/articles/Untitled_Item/5472451). More details on the 136-th Cruise  
 590 of the RRS “James Cook” can be found at <https://deeplinksproject.wordpress.com/> and  
 591 [https://www.bodc.ac.uk/resources/inventories/cruise\\_inventory/report/16050/](https://www.bodc.ac.uk/resources/inventories/cruise_inventory/report/16050/). We

592 are very grateful to the Chief Editor, Associate Editor and two Reviewers for their sup-  
593 portive comments, which helped us to focus the manuscript.

## References

- 594 Abarbanel, H.D., D.D. Holm, J.E. Marsden, and T. Ratiu (1984), Richardson number  
595 criterion for the nonlinearity of 3D stratified flow. *Phys. Rev. Lett.*, 52, 2352-2355.
- 596 Aleinik, D.D., G.I. Shapiro, L.D. Mee, and E.M. Lemesko (2007), Using a lowered acous-  
597 tic doppler current profiler for measuring current velocities in the Black Sea. *Oceanology*,  
598 47(1), 127-137.
- 599 Baines, P.G. (1982), On internal tide generation models. *Deep Sea Res. I*, 29 (3A), 307-  
600 339.
- 601 Baines, P.G. (2007), Internal tide generation by seamounts. *Deep Sea Res. I*, 54(9), 1486-  
602 1508, doi:10.1016/dsr.2007.05.009.
- 603 Egbert, G.D., and S.Y. Erofeeva (2002), Efficient inverse modeling of barotropic ocean  
604 tides, *J. Atmos. Oceanic Technol.*, 19(2), 183-204.
- 605 Flexas, M. M., M. P. Schodlok<sup>1</sup>, L. Padman, D. Menemenlis<sup>1</sup>, and A. H. Orsi (2015),  
606 Role of tides on the formation of the Antarctic Slope Front at the Weddell-Scotia Con-  
607 fluence, *J. Geophys. Res.*, 120, 36583680, doi:10.1002/2014JC010372.
- 608 Gerkema, T. (2001), Internal and interfacial tides: beam scattering and local generation  
609 of solitary waves. *J. Mar. Res.* 59, 227-255.
- 610 Haidvogel, D.B., A. Beckmann, D.C. Chapman, and R.-Q. Lin (1993), Numerical simu-  
611 lation of flow around a tall isolated seamount. Part II: Resonant Generation of trapped  
612 waves. *J. Phys. Oceanogr.*, 23, 2373-2391.

- 613 Henry, L.-A., J. Vad, H. S. Findlay, J. Murillo, R. Miligan, and J. M. Roberts (2014), Envi-  
614 ronmental variability and biodiversity of megabentos on the Hebrides Terrace Seamount  
615 (Northeast Atlantic), *Sci. Rep.*, *4*, 5589, doi:10.1038/srep05589(2014).
- 616 Howard, L.N. (1961), A note on the paper of John W. Miles. *J. Fluid Mech.*, *10*, 509-512.
- 617 Huthnance, J.M.(1973), Tidal current asymmetries over the Norfolk sandbanks. *Estuar.*  
618 *Coastal Mar. Sci.*, *1*, 89-99.
- 619 Larsson, A.J., J. Järnegren, S.M. Strömberg, M.P. Dahl, T. Lundälv, and S. Brooke (2014)  
620 Embryogenesis and larval biology of cold-water coral *Lophelia pertusa*, *PLoS ONE*, *9*(7),  
621 e102222, doi:101371/journal.pone.0102222.
- 622 Lavelle, J.W., and C. Mohn (2010), Motion, commotion, and biophysical connections at  
623 deep ocean seamounts. *Oceanography*, *23*(1), 91–103.
- 624 Loder, J.W. (1980), Topographic rectification of tidal currents on the sides of Georges  
625 Bank. *J. Phys. Oceanogr.*, *10*, 1399-1416.
- 626 Marshall, J., A. Adcroft, C. Hill, L. Perelman, and C. Heisey (1997), A finite-volume,  
627 incompressible Navier-Stokes model for studies of the ocean on the parallel computers,  
628 *J. Geophys. Res.*, *102*, 5733–5752.
- 629 Miles, J.W. (1961), On stability of heterogeneous shear flows. *J. Fluid Mech.*, *10*, 496-508.
- 630 Morato, T., S. D. Hoyle, V. Allain, and S. J. Nical (2010), Seamounts are  
631 hotspots of pelagic biodiversity in the open ocean, *PNAS*, *107*(21), 9707–9711,  
632 doi:10.1073/pnas.0910290107.
- 633 Rogers, A. (1994), The biology of Seamounts, *Advances in Marine Biology*, *30*, 305–351.
- 634 Pacanowski, R.C., and S. G. H. Philander (1981), Parametrisation of vertical mixing in  
635 numerical models of Tropical Oceans, *J. Phys. Oceanogr.*, *11*, 1443-1451.



- 636 Pingree, R.D., and L. Maddock (1980), Tidally induced residual flows around an island  
637 due to both frictional and rotational effects, *J. Geophys. J. R. Astr. Soc.*, *63*, 533–546.
- 638 Pingree, R.D., and G.T. Mardell (1981), Slope turbulence, internal waves and phytoplank-  
639 ton growth at the Celtic Sea shelf-break, *Phil. Trans. R. Soc. Lond. A*, *302*, 663-682.
- 640 Pingree, R.D., and G.T. Mardell (1985) Solitary internal waves in the Celtic Sea. *Prog.*  
641 *Oceanogr.*, *14*, 431-441.
- 642 Sherwin, T.J., D. Aleynik, E. Dumont, and M.E. Inall (2015), Deep drivers of mesoscale  
643 circulation in the central Rockall Trough. *Ocean Sci.*, *11*, 349–359.
- 644 Stashchuk, N., and K. Hutter (2001), Modelling of water exchange through the Strait of  
645 the Dardanelles. *Cont. Shelf. Res.*, *21*, 1361-1382.
- 646 Stashchuk, N., Vlasenko, V., P. Hosegood, and A. Nimmo-Smith (2017), Tidally induced  
647 residual current over the Malin Sea continental slope. *Cont. Shelf. Res.*, *139*, 21-34.
- 648 Stashchuk, N., Vlasenko, V., M.E. Inall, and D. Aleyinik (2014), Horizontal dispersion in  
649 shelf seas: High resolution modelling as an aid to sparse sampling. *Progr. Oceanogr.*,  
650 *128*, 74-87.
- 651 Visbeck, M. (2002), Deep velocity profiling using lowered acoustic Doppler current profil-  
652 ers: bottom track and inverse solutions. *J. Atmos. and Ocean Tech.*, *19*,794–807.
- 653 Vlasenko, V. (1994), Multimodal soliton of internal waves. *Izvestiya Atmospheric and*  
654 *Oceanic Physics* , *30(2)*, 161–169.
- 655 Vlasenko, V., and N. Stashchuk (2006), Amplification and suppression of internal waves  
656 by tides over variable bottom topography. *J. of Phys. Oceanogr.*, *36(10)*, 1959–1973.
- 657 Vlasenko, V., and N. Stashchuk (2015), Internal tides near the Celtic Sea shelf  
658 break: A new look at a well known problem. *Deep Sea Res.I*, *103*, 24–36,

659 doi:10.1016/dsr.2015.05.003.

660 Vlasenko, V., N. Stashchuk, M.R. Palmer, and M.E. Inall (2013), Generation of baroclinic  
661 tides over an isolated underwater bank. *J. Geophys. Res.*, 118(9), 4395-4408.

662 Vlasenko V., N. Stashchuk, and K. Hutter (2005), Baroclinic tides: theoretical modeling  
663 and observational evidence. Cambridge University Press. 365 pp.

664 Vlasenko V., N. Stashchuk, M. E. Inall, and J. Hopkins (2014), Tidal energy conversion in  
665 a global hot spot: on the 3D dynamics of baroclinic tides at the Celtic Sea shelf break,  
666 *J. Geophys. Res.*, 119(6), 3249–3265, doi:10.1002/2013JC009708.

667 Vlasenko V., N. Stashchuk, M. E. Inall, M. Porter, and D. Aleynik (2016), Fo-  
668 cusing of baroclinic tidal energy in a canyon. *J. Geophys. Res. Oceans*, 121,  
669 doi:10.1002/2015JC011314.

670 Wessel, P., D.T. Sandwell, and S.-S. Kim (2010), The global seamount census. *Oceanog-*  
671 *raphy*, 23(1), 24–33.

672 Young, W.R., P.B. Rhines, and C.J.R. Garrett (1982), Shear-flow dispersion, internal  
673 waves and horizontal mixing in the ocean. *J. of Phys. Oceanogr.*, 12, 515-527.

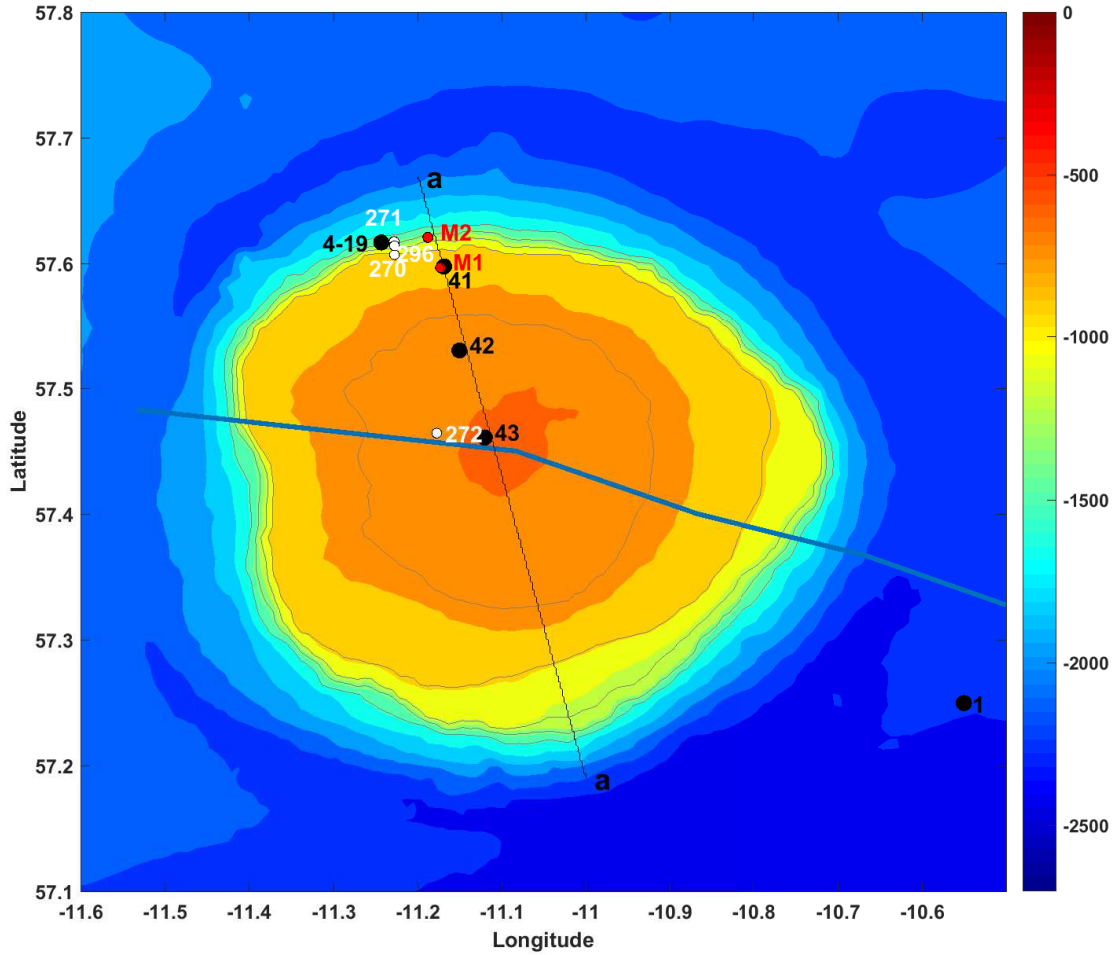


**Figure 1.** Topography of ADS with positions of CTD stations (black), moorings (red), and ROV dives (white dots). The Ellett Line along which regular CTD surveys have been conducted since 1975 is shown by the blue line ([www.o-snap.org](http://www.o-snap.org)). The thin solid line (a-a) shows the transect used for the analysis of the model output.

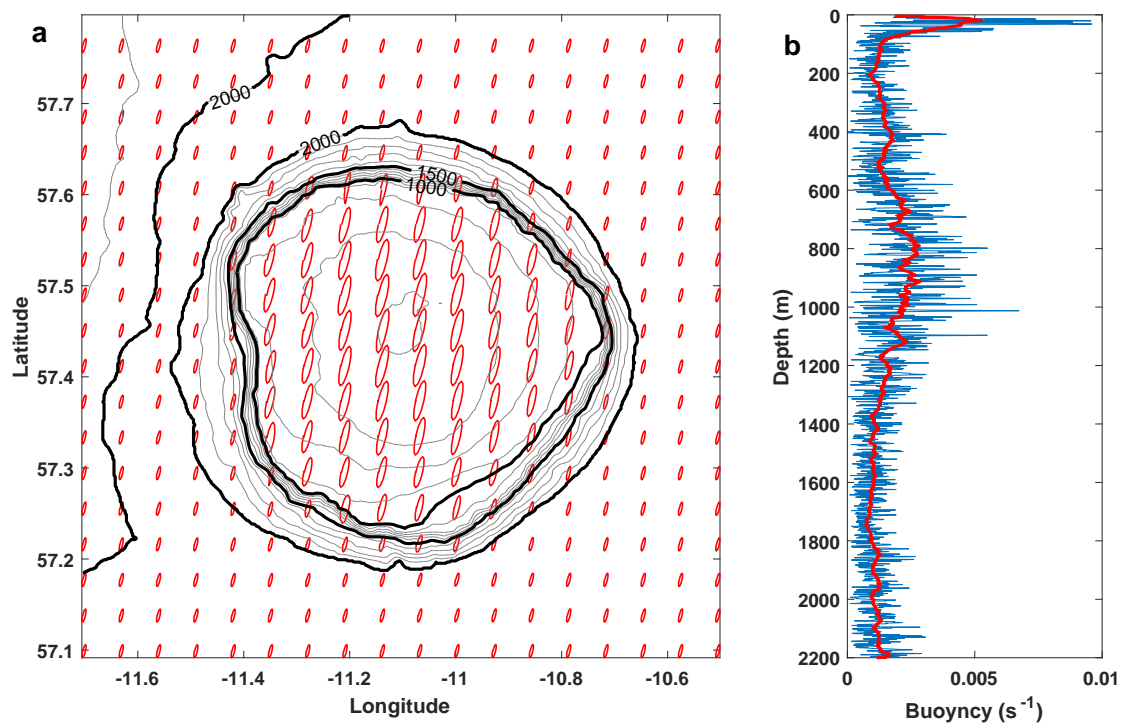


**Figure 2.** a) Tidal ellipses in the area of ADS predicted by the TPX08.1 inverse tidal model. b) Instant (blue) and smoothed (red) buoyancy frequency profiles recorded at CTD station 1.

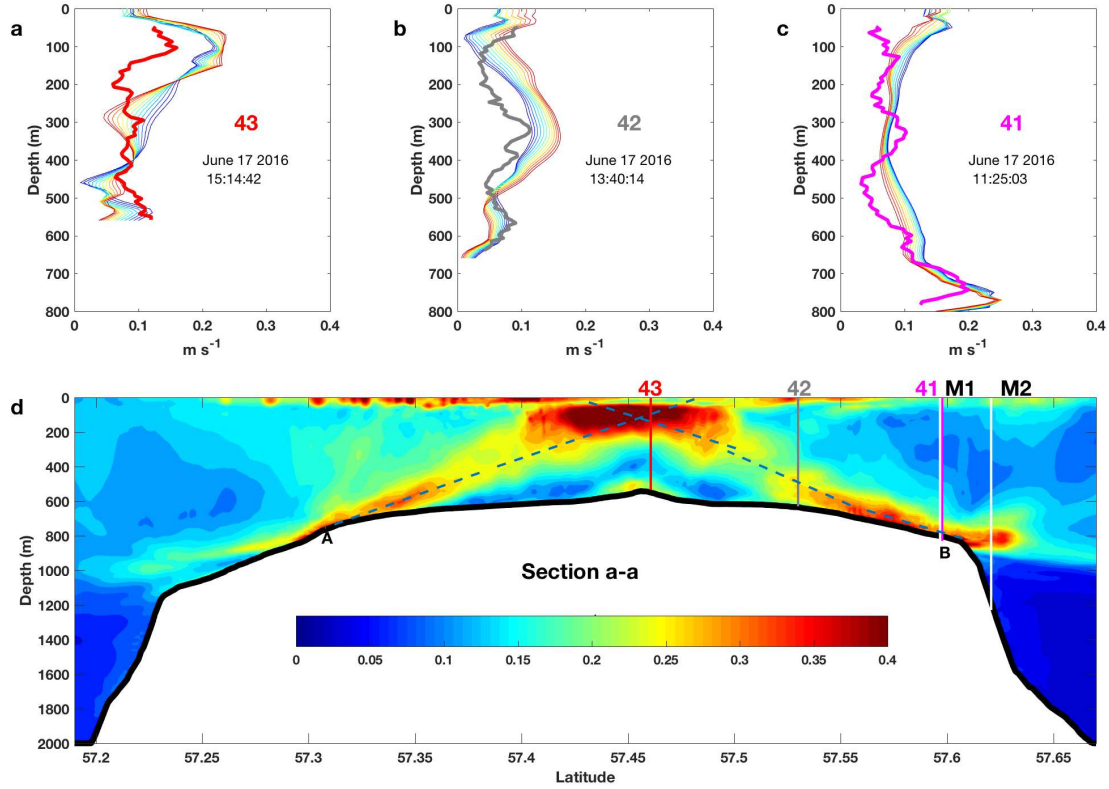


**Figure 3.** (a-c) Profiles of the horizontal velocity amplitude  $\sqrt{u^2 + v^2}$  at CTD stations 41-43. Thick lines represent the in-situ recorded profiles, thin coloured lines depict the model predicted curves with five minutes temporal interval starting from the time of real CTD sampling. (d) Model predicted amplitudes of horizontal velocities in the cross-section a-a, Figure 1. Positions of the CTD stations 41-43 and moorings M1 and M2 are shown by vertical lines. Dashed curves depict the positions of tidal beams.

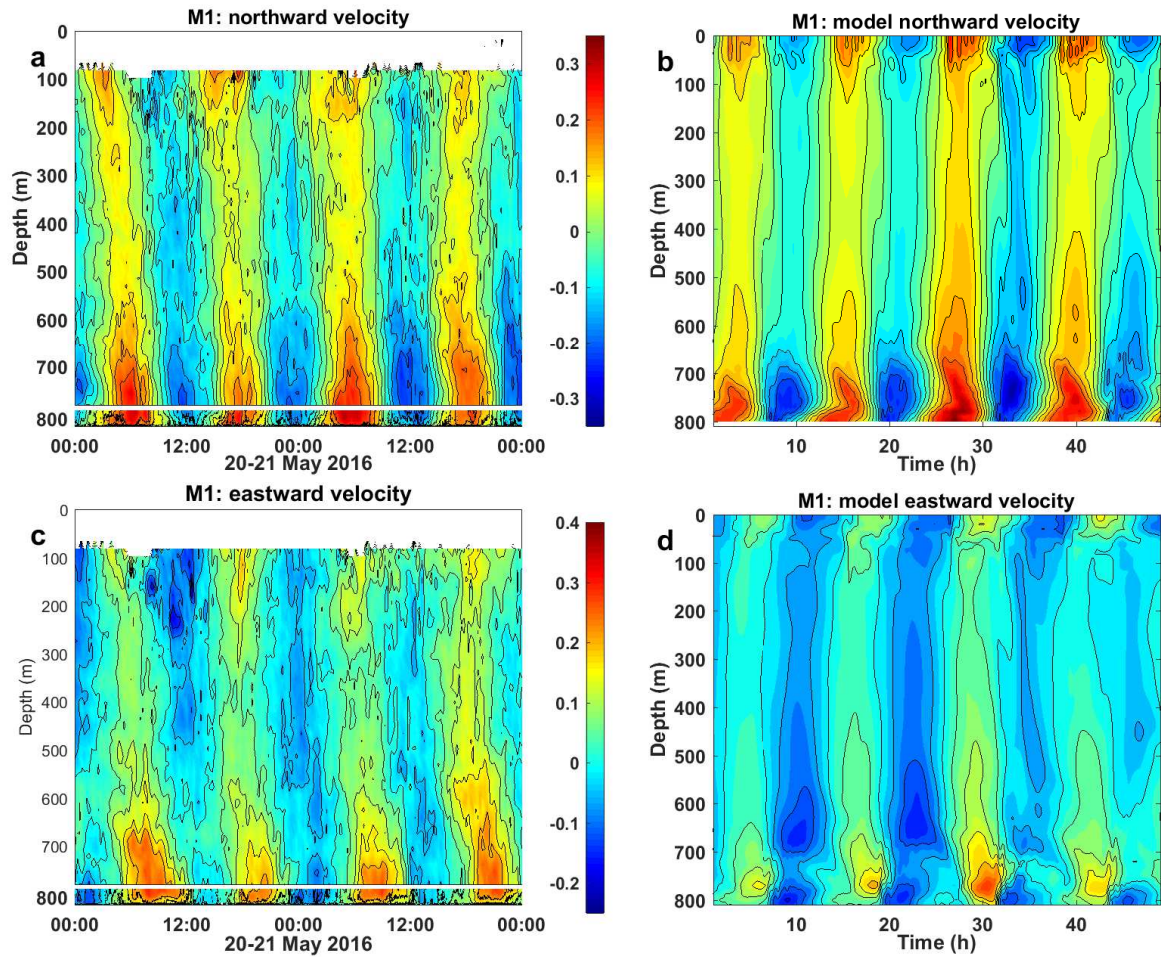


**Figure 4.** Two day time series of zonal (a,c) and meridional (b,d) velocities recorded at mooring M1 (left column) and predicted by the model (right column).

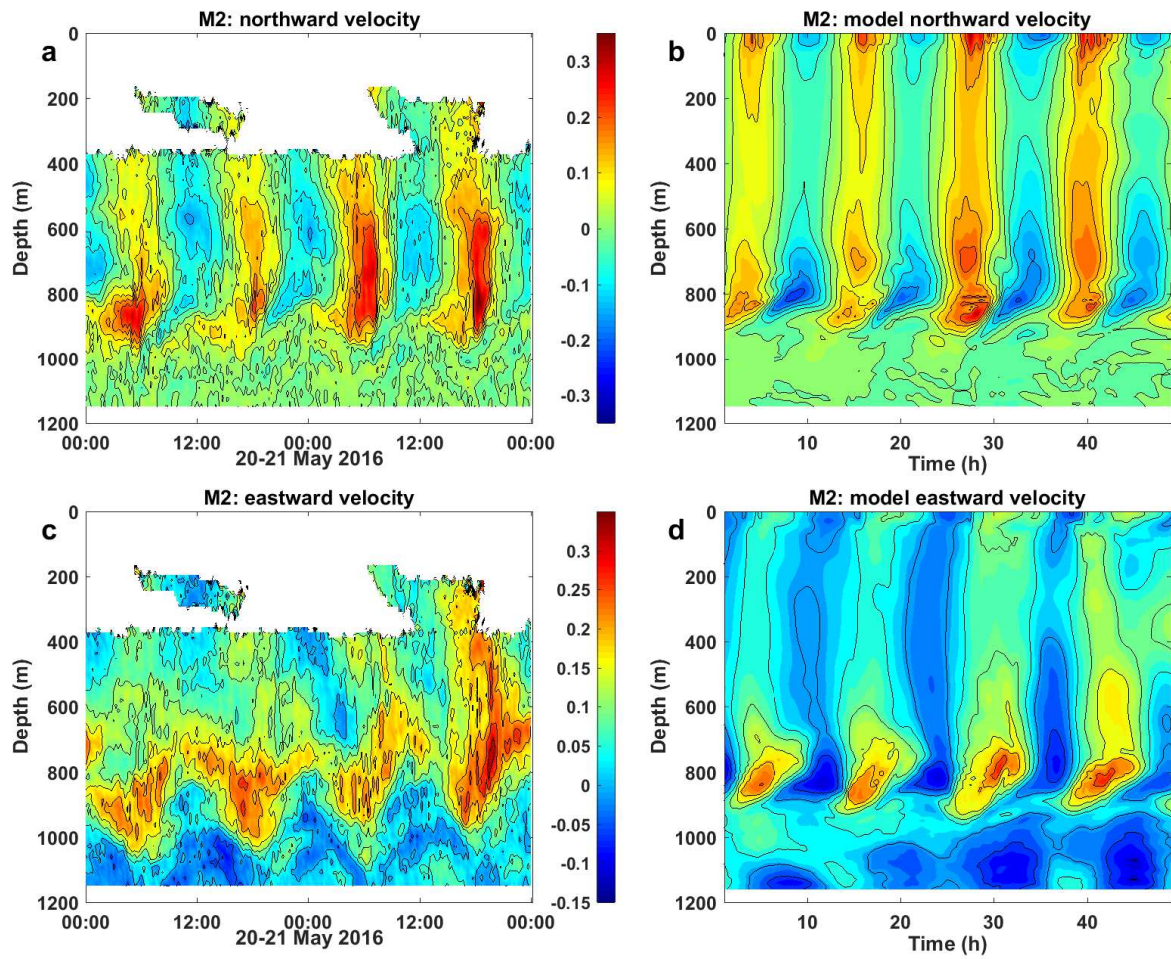


**Figure 5.** The same as in Figure 4 but for mooring M2.

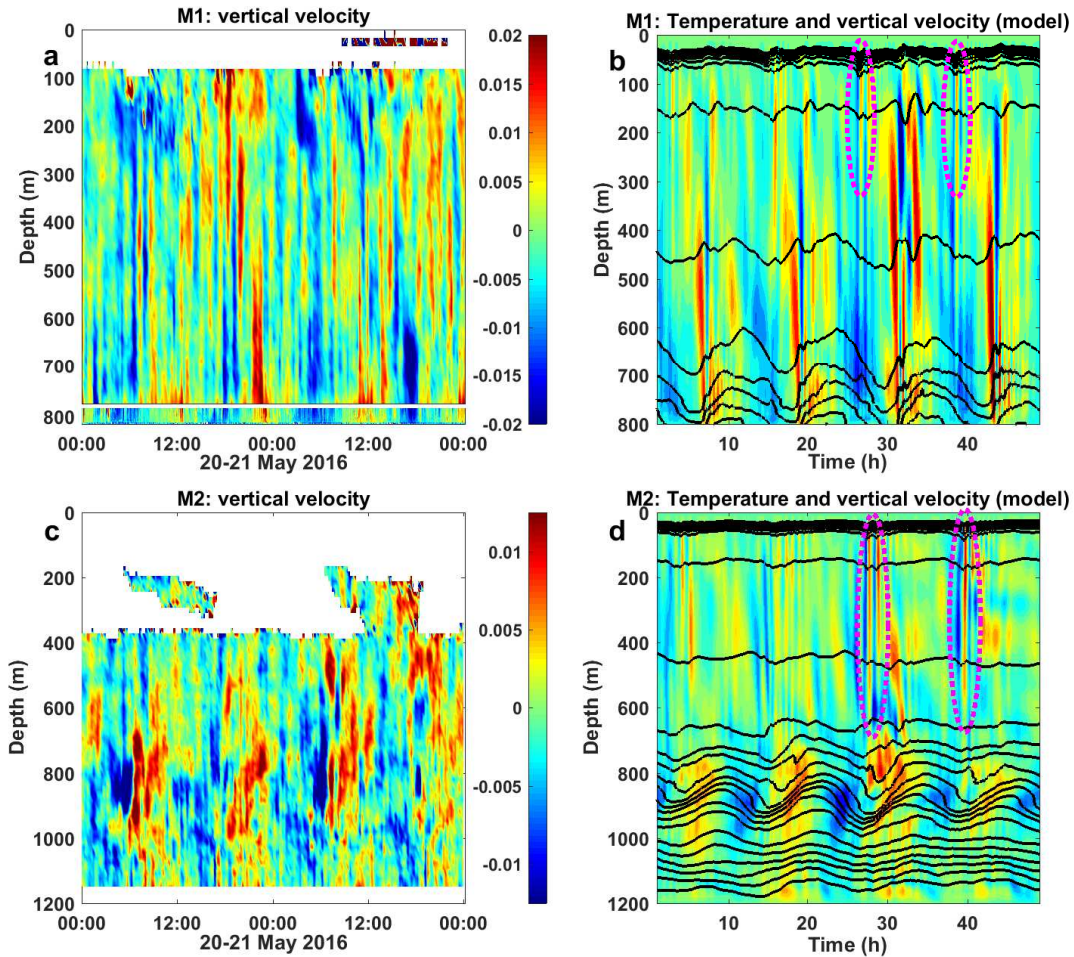


**Figure 6.** Vertical velocities recorded at moorings M1 and M2 (left) and reproduced by the model (right). The model predicted velocities are overlaid with the temperature field. Red dotted ellipses in panels b and d show the packets of short-scale internal waves.



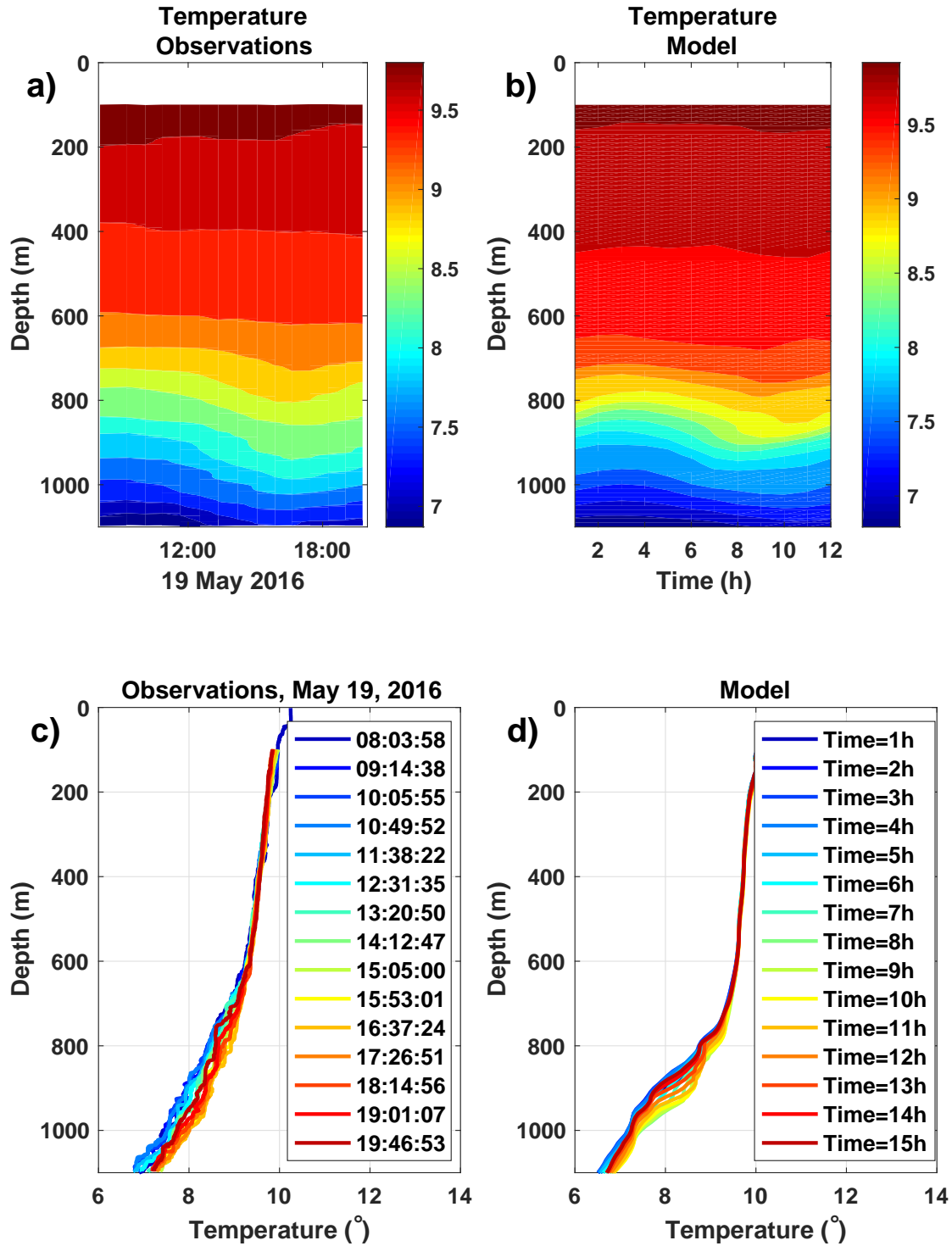


**Figure 7.** Observational (a) and model predicted (b) temperature time series recorded at the yo-yo CTD station on 19th May 2016. Temperature profiles for the yo-yo station position recorded in-situ (c) and predicted by the model (d).

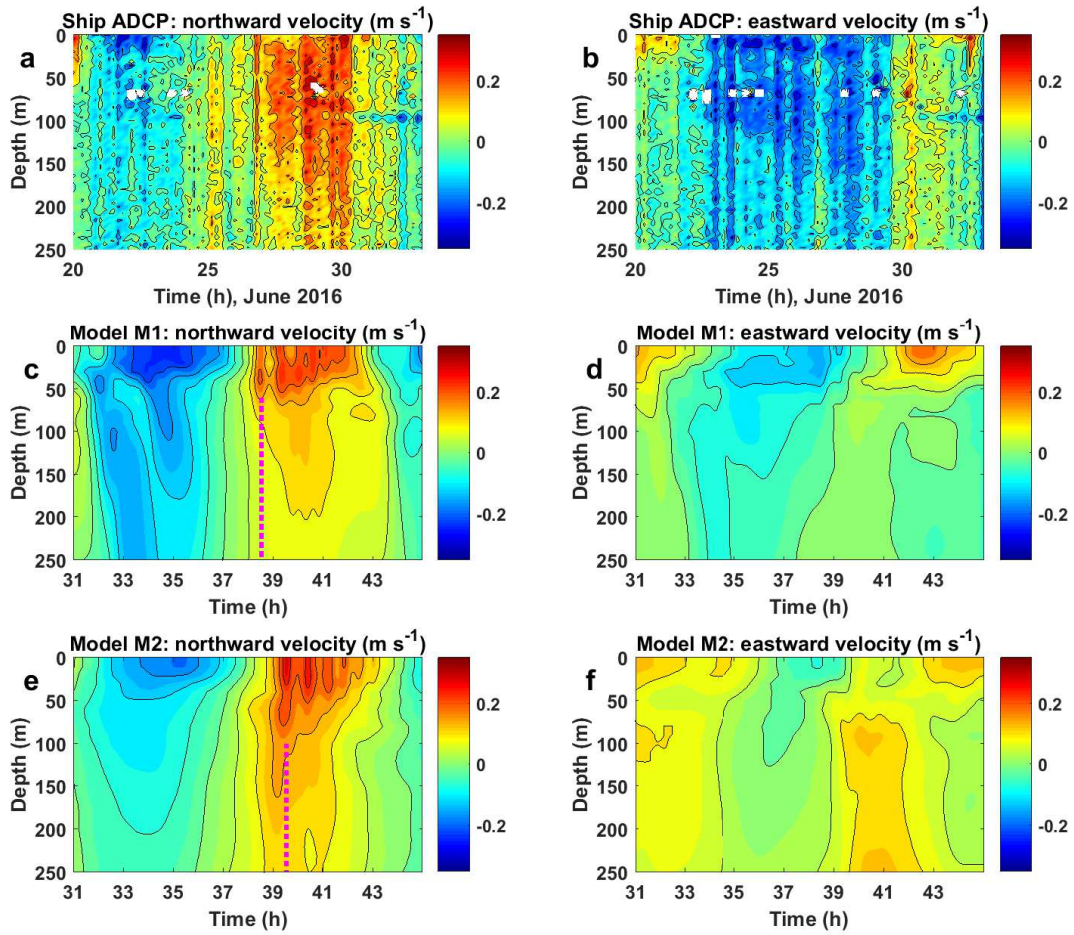


**Figure 8.** Meridional (left column) and zonal (right column) velocities recorded by the ship mounted ADCP during ROV dive 296 (panels a and b) and predicted by the model (panels c, d, e, and f) at the positions of M1 and M2 moorings during the ROV dive.

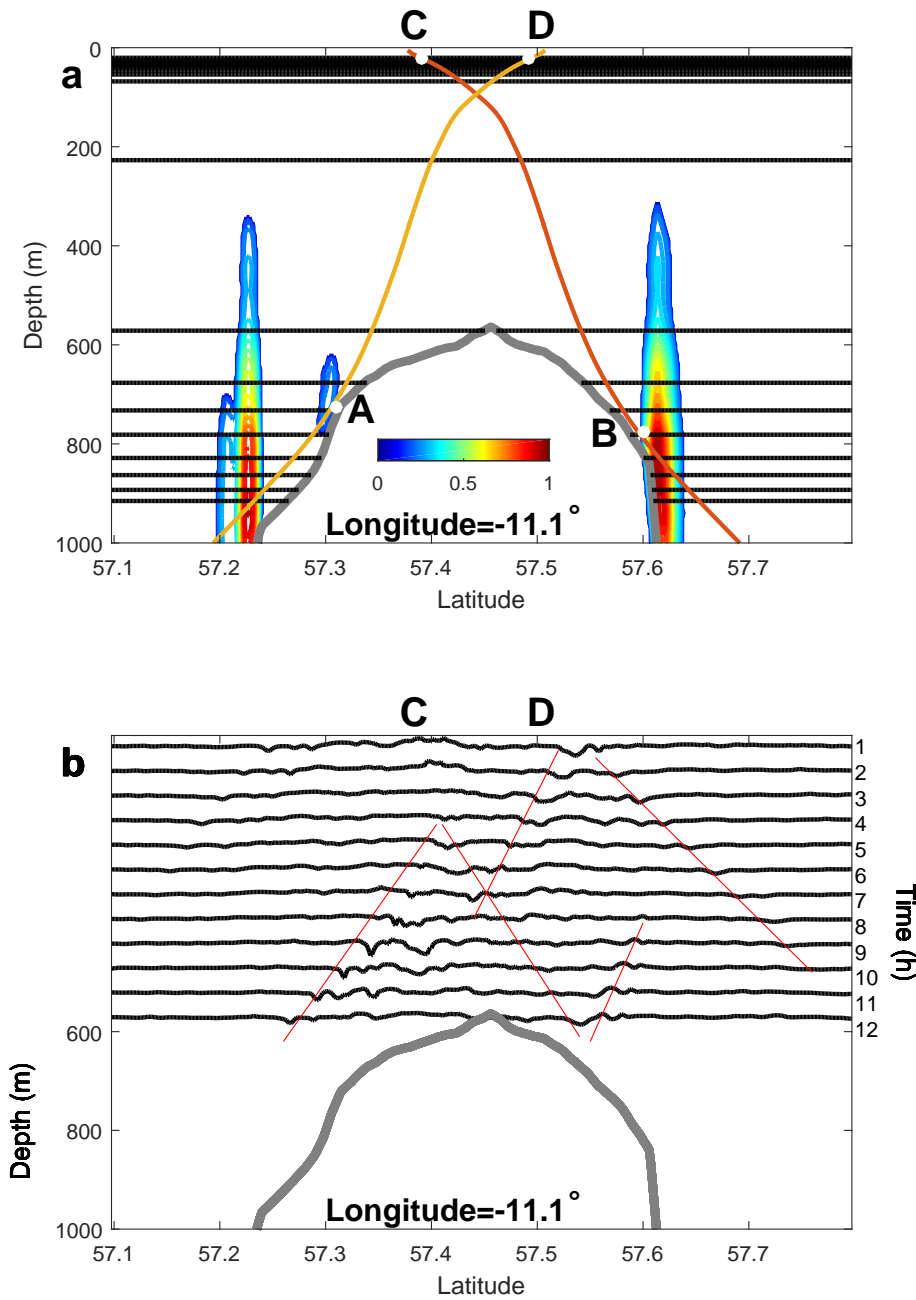


**Figure 9.** a) Meridional 11.1°W cross-section of undisturbed temperature field through the ADC summit. The interval between isotherms equals 0.25 °C. Contours AD and BC are characteristic lines (3). Vertically oriented coloured zones show positions of the maxima of normalized IBF (5). b) Hovmöller diagram showing evolution of isotherm 12° along the longitude 11.1°W. Time interval between contours equals 1 hour. The red lines depict the positions of wave packets.

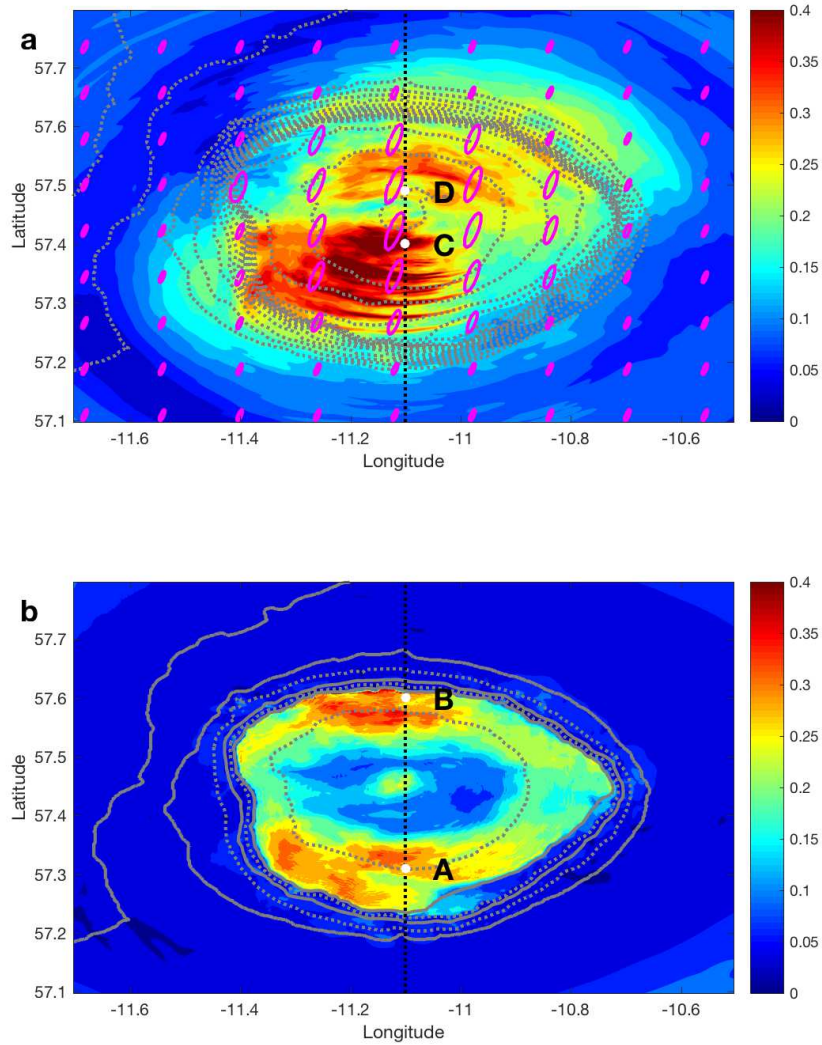


**Figure 10.** Amplitude of horizontal velocity  $\sqrt{u^2 + v^2}$  (ms<sup>-1</sup>) at the free surface (a) and 10 m above the bottom (b). Position of the 11.1°W section is shown by the dashed line. Points A, B, C and D correspond to those shown in Fig. 9.

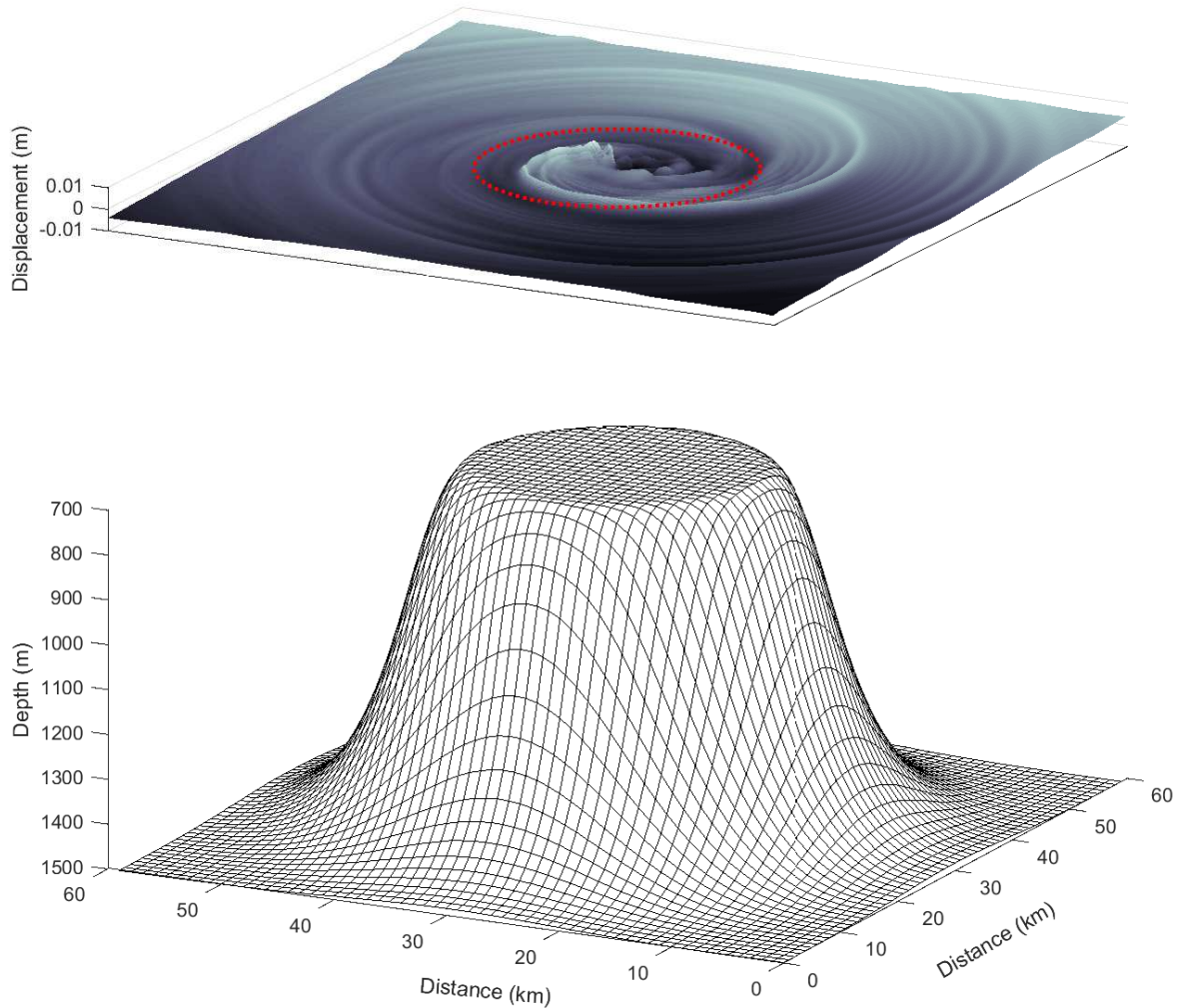


**Figure 11.** Sea surface displacements produced by internal waves over an isolated symmetrical table seamount. Surface elevations and depressions are shown by white and black colors, respectively. Red dotted line represents a central (flat) part of the bank depicted in the bottom panel.

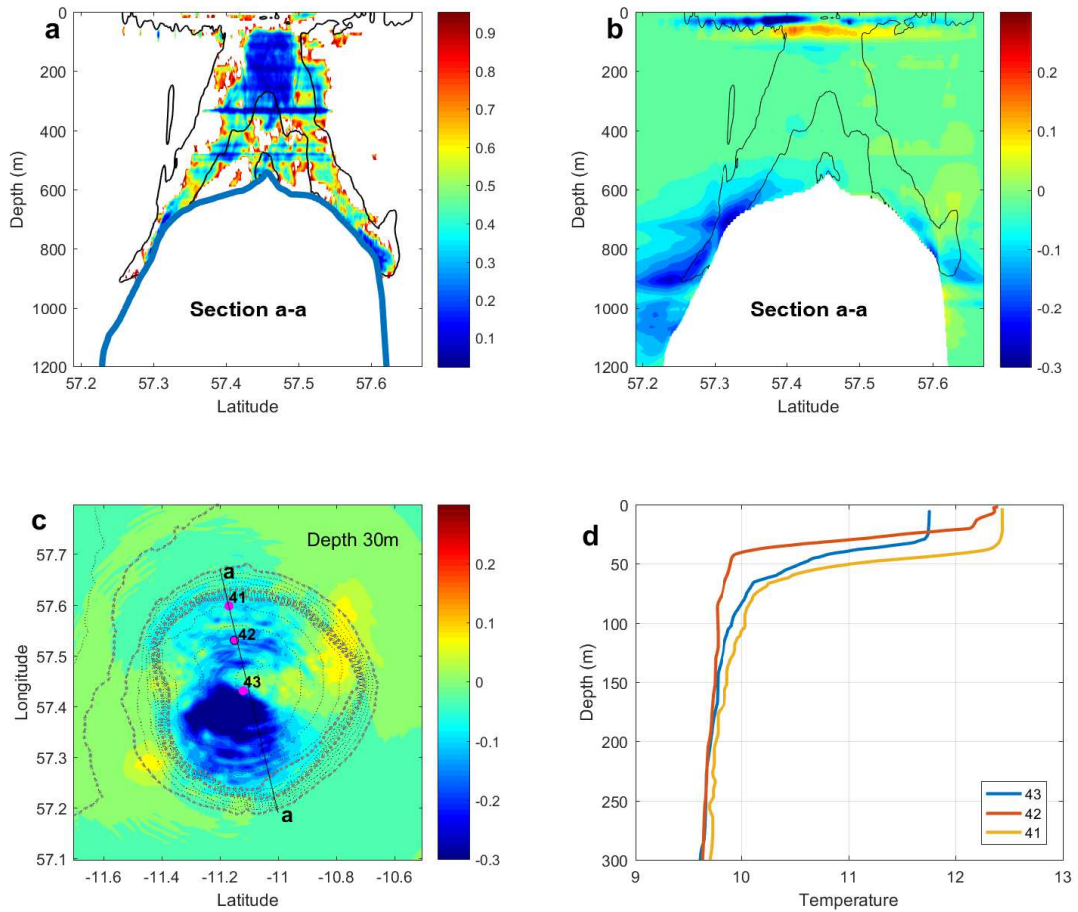


**Figure 12.** a) Model predicted minimum value of the Richardson number over a tidal period at the transect a-a shown in panels c). b) Difference between initial temperature and that modified by internal wave mixing. The solid black lines in panel a) and b) show velocity magnitude  $0.2 \text{ ms}^{-1}$ . c) Temperature field modifications induced by internal waves in the surface layer. d) Vertical temperature profile recorded at CTD stations 41-43.

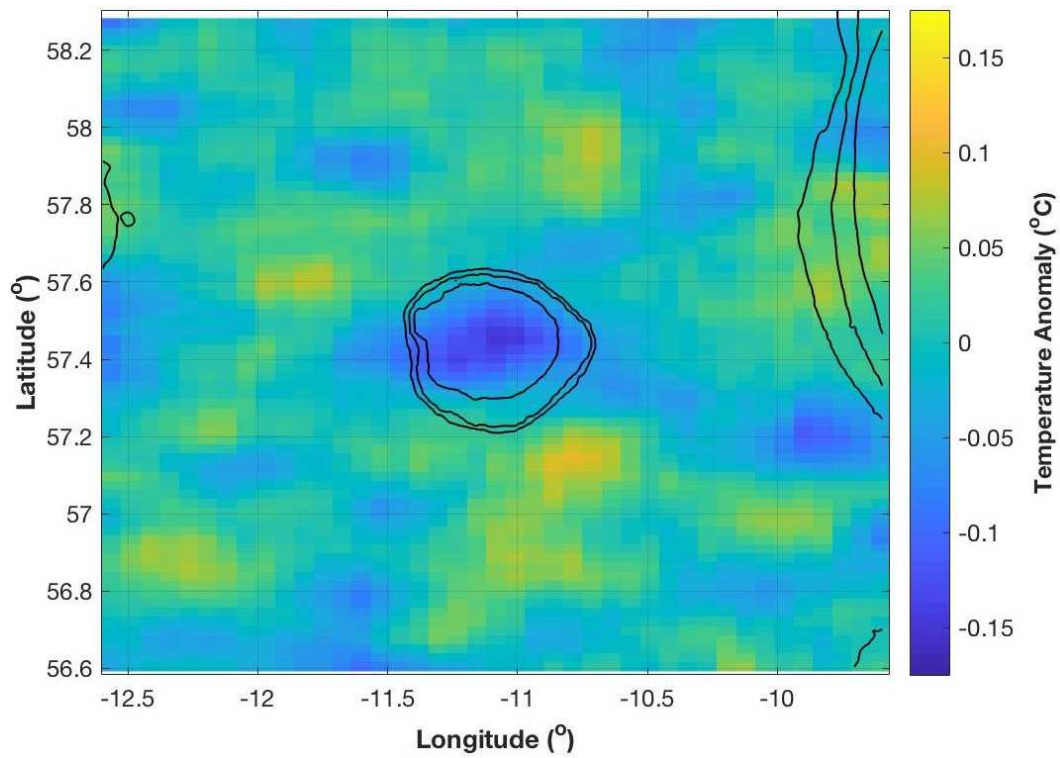


**Figure 13.** Deviation of the sea surface temperature (SST) from an average SST recorded by MODIS-Aqua satellite in May - August 2003-2016. Large-scale zonal and meridional gradients have been subtracted using a two-dimensional third-order polynomial.



**Figure 14.** a) Model predicted residual currents generated over ADS at 500-m depth. The velocity fields were averaged over five tidal cycles. The black line with dots shows the Ellet Line. Residual zonal (b) and meridional (c) velocities along the Ellet Line predicted by the model.



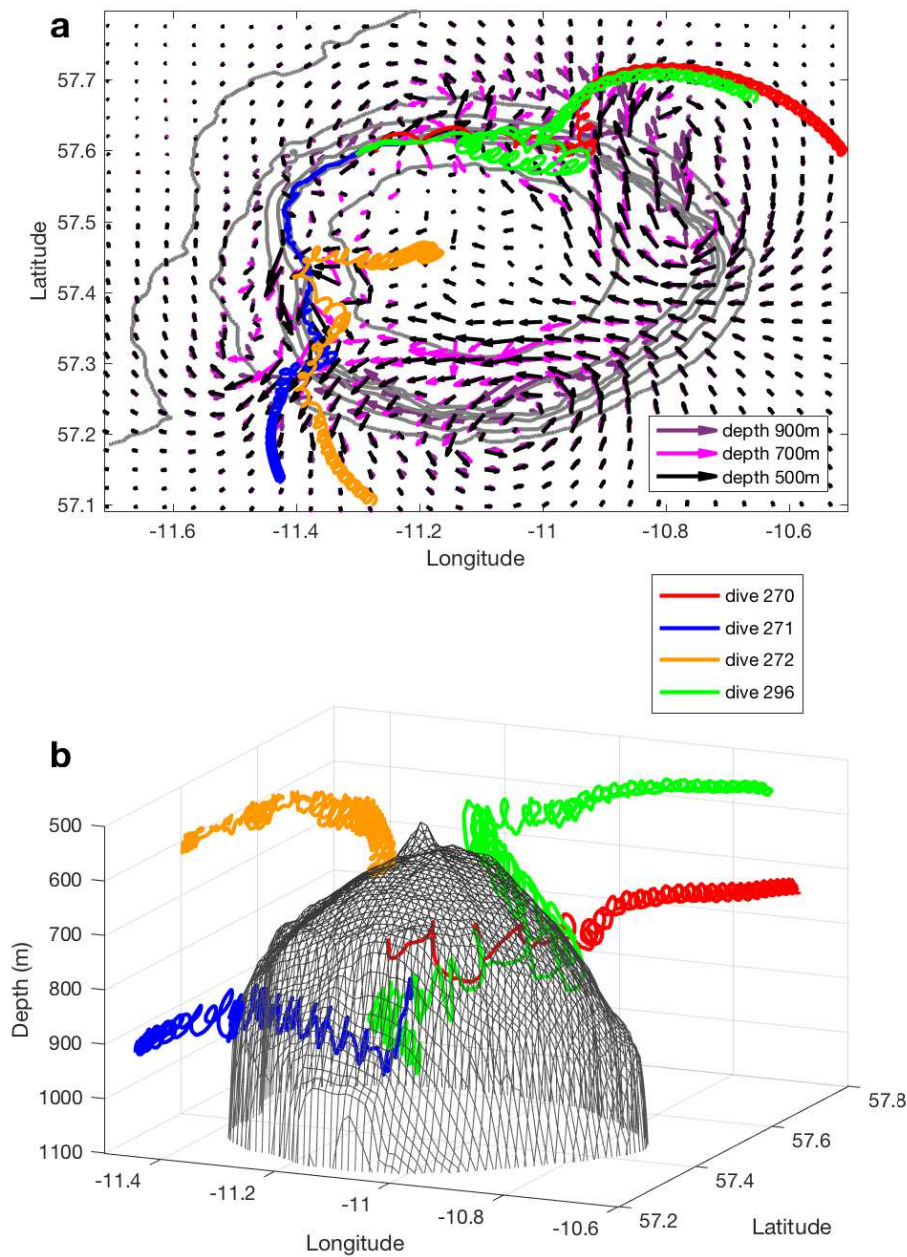


**Figure 15.** a) Plan view of the trajectories of the particles overlapped with the field of residual currents. b) Three dimensional projection of the particle trajectories.

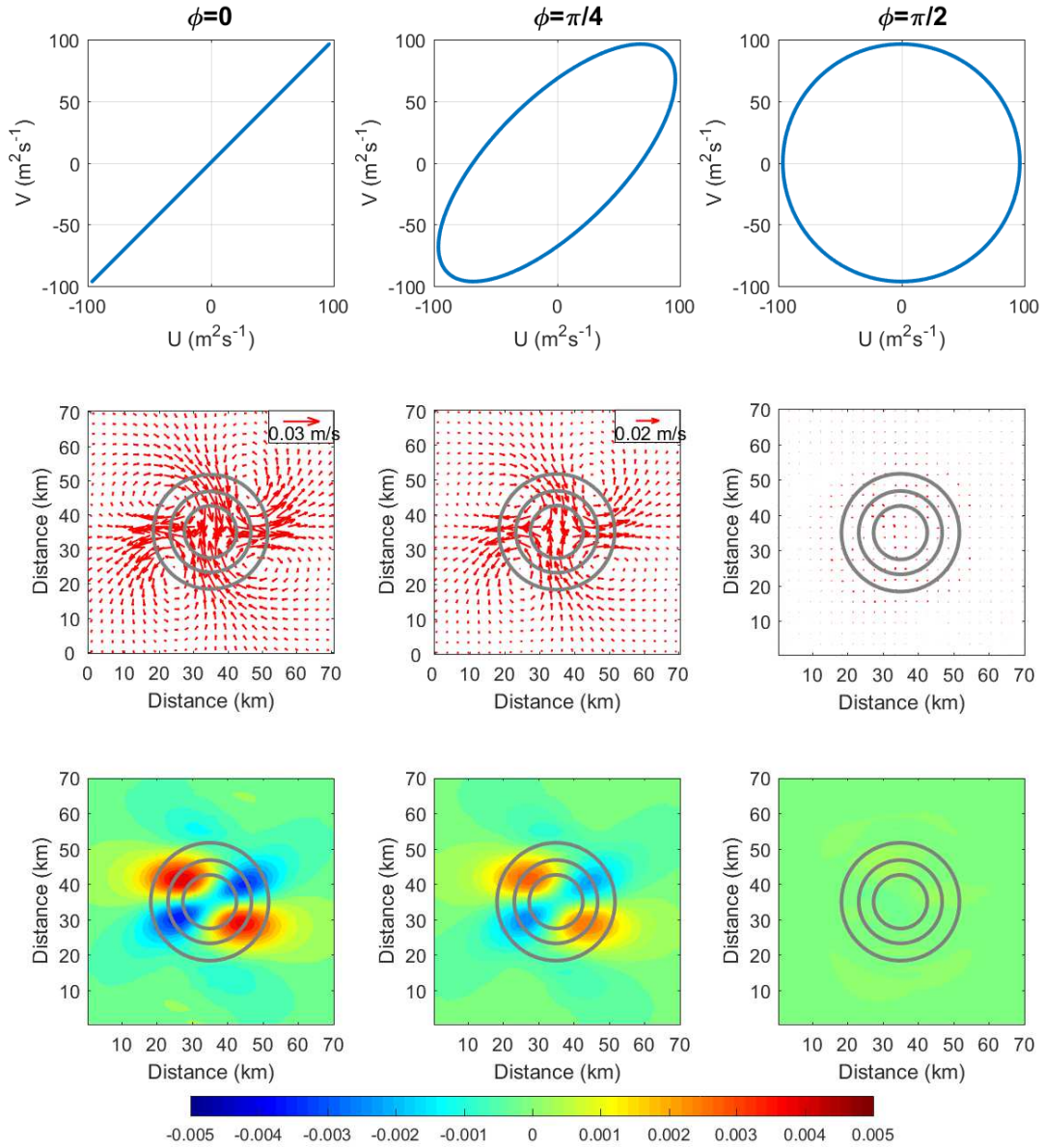


**Figure A.1.** Residual currents generated by tide over the Gaussian bank (A1) for  $A = B = 100\text{m}^2\text{s}^{-1}$  and  $\phi = 0$  (left column),  $\phi = \pi/4$  (middle column), and  $\phi = \pi/2$  (right column). Top row shows the tidal ellipses expressed in terms of water discharge. Middle panels represent the spatial distributions of residual currents. Bottom panels depict the vorticity  $u_y - v_x$  ( $\text{s}^{-1}$ ).

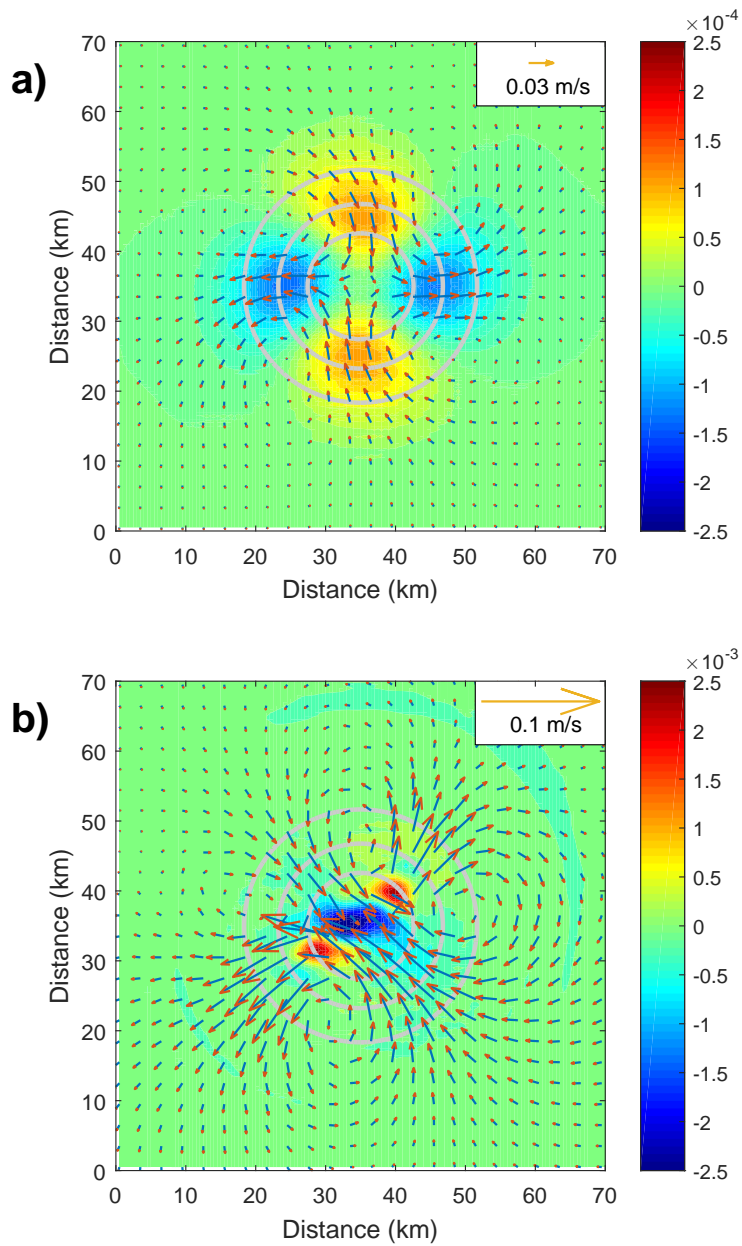


**Figure A.2.** Spatial distribution of residual currents shown by arrows overlaid with the vertical velocity at the depth of 600 m obtained for homogeneous (a) and stratified (b) fluids.

**Table 1.** Moorings

Moorings	Longitude	Latitude	Water depth (m)	Frequency (kHz)
M1 (up)	11°10.352'W	57°35.803'N	770	75
M1 (dn)	11°10.352'W	57°35.803'N	780	600
M2 (up)	11°11.250'W	57°37.242'N	1160	75
M2 (dn)	11°11.250'W	57°37.242'N	1170	600

**Table 2.** Positions of the ROV dives

Dive	Longitude	Latitude	Water depth (m)
270	11°16.062'W	57°35.838'N	826.8
271	11°14.388'W	57°36.504'N	928.3
272	11°10.980'W	57°26.98'N	645.2
296	11°13.590'W	57°36.66'N	1065.2